On the constitutive relationship between solidification cells and the fatigue behaviour of IN718 fabricated by laser powder bed fusion

Alessandro Piglione[1,*], Bonnie Attard[2,3], Vitor Vieira Rielli[4], Claudia-Tatiana Santos Maldonado[1], Moataz M. Attallah[2], Sophie Primig[4], Minh-Son Pham[1]

[1]Department of Materials, Imperial College London, Exhibition Road, London SW7 2AZ, UK
[2]School of Metallurgy and Materials, University of Birmingham, Edgbaston, Birmingham B15 2TT, UK
[3]Department of Metallurgy and Materials Engineering, Faculty of Engineering, University of Malta, Imsida MSD 2080, Malta
[4]School of Materials Science & Engineering, UNSW Sydney, NSW 2052, Australia

*Corresponding author.
E-mail address: alessandro.piglione16@imperial.ac.uk
Phone: +44 20 7594 9529

Keywords: Laser powder bed fusion, IN718, fatigue, solidification cells, cyclic plasticity

ABSTRACT

IN718 combines excellent mechanical properties with a good weldability and is therefore an ideal alloy for laser powder bed fusion (LPBF). Knowledge of the relationship between its as-built microstructure, particularly solidification cells, and its fatigue properties is needed to better utilise additively manufactured microstructures and guide their further optimisation. This study presents a comprehensive investigation of the as-built microstructure and the associated monotonic and fatigue properties of LPBF IN718 aimed at highlighting the influential effect of solidification cells on monotonic and cyclic plasticity. In monotonic tension, cells induced pronounced strain hardening and good ductility by acting as strong yet not impenetrable obstacles to dislocation slip. In fatigue loading, cyclic hardening followed by cyclic softening was linked to the stability of the as-built solidification cells, the high initial

dislocation densities and the subsequent rearrangements of such dislocations during cyclic loading using the similitude relation and the evolution of friction and back stresses. By thoroughly investigating the evolution of the cyclic response of samples printed using two different scanning patterns, the relationship between process (scanning line length and thus local substrate temperature), microstructure (dislocation cell size and their spatial arrangement) and mechanical properties (cyclic hardening and softening responses) was comprehensively discussed.

1 INTRODUCTION

IN718 is a precipitation-hardened (Ni, Fe)-based polycrystalline superalloy that is extensively used for gas and steam turbine components such as turbine discs and drive shafts in aeroengines and power generation plants [1–4]. Its attractiveness lies in its excellent mechanical properties at elevated temperatures up to 650 °C, coupled with a good resistance to aggressive environments [2,3,5,6]. IN718 relies on the formation of coherent γ" and γ' precipitates through a double ageing treatment as its main strengthening mechanism. Although conventionally processed by either casting or forging depending on the expected loads [3–5], IN718 is regarded as a suitable alloy for metal additive manufacturing (AM) thanks to its excellent weldability, which stems from the slow precipitation kinetics of its main strengthening precipitate γ" [2,6,7]. Due to the alloy's wide applicability, its promising weldability and the potential advantages arising from AM processes, several studies have been devoted to the investigation of the solidification microstructures and properties of IN718 fabricated by AM, and in particular by laser powder bed fusion (LPBF) (e.g., [4,8–12]).

Whilst the static mechanical properties of AM alloys are often found to be comparable or even superior to those of their conventionally-manufactured counterparts, their poor fatigue performance is one of the key factors limiting their widespread applicability [13–16]. Hence, a number of studies have assessed the fatigue performance of LPBF IN718 [13,15–27]. The majority of these studies, however, have investigated the alloy's fatigue properties after post-processing treatments, such as heat treatments and

hot isostatic pressing [13,15,17,19–21,23–27], and very few studies have studied the alloy's fatigue performance in the as-built condition [16,18,22,28]. This is due to the fact that as-built LPBF IN718 does not feature strengthening precipitates [10,28,29]; hence, heat treatments are required to achieve the alloy's best mechanical performance for practical applications. However, LPBF IN718 requires dedicated heat treatments due to its peculiar as-built microstructures; the design of such heat treatments relies on a thorough understanding of the relationship between the alloys' microstructure and its fatigue properties. In particular, as-built LPBF alloys feature fine sub-grain solidification cells with high dislocation densities at cell boundaries [11,30–33], which have been shown to have a dramatic beneficial impact on the monotonic strength of LPBF alloys without affecting their ductility [34–36]. As a consequence, the retainment of solidification cells has been identified as a key requirement of heat treatments for LPBF IN718 aimed at optimising its monotonic performance [10]. Solidification cells are expected to significantly impact also the fatigue properties of LPBF IN718, but dedicated studies have not been carried out yet; there is therefore a strong need to understand the influence of solidification cells on the development of cyclic plasticity and thereby guide microstructure design (e.g., via heat treatment) to improve the alloy's fatigue performance. Such investigation is best carried out on as-built samples, as heat treatments would induce the precipitation of strengthening precipitates, thereby making the deconvolution of each individual contribution more challenging, as well as potentially affect dislocation arrangements at cell boundaries.

Therefore, this work presents a comprehensive investigation of the as-built solidification cellular microstructure and an in-depth discussion of its relationship with the fatigue behaviour of as-built LPFB IN718 at room temperature. Particular attention is devoted to the stability of solidification cells and to their interactions with mobile dislocations, which govern the development of cyclic plasticity and thereby the evolution of the alloy's response during cyclic loading. In addition, two distinct scanning patterns are employed to investigate the effect of process parameters on as-built microstructures, and particularly on solidification cells, and to subsequently relate such differences to the distinct cyclic responses of the samples. The investigation of the alloy's monotonic properties at room temperature is also included to complement that of its fatigue properties.

2 MATERIALS AND METHODS

Pre-alloyed gas atomised IN718 powder was provided by Höganäs; the powder's nominal composition is provided in Table 1. The powder particle size range was 15 – 45 µm. Cuboidal bars measuring 140x24x22 mm^3 were manufactured with a Concept Laser M2 laser powder bed fusion (LPBF) system. Such bars were printed using either a bidirectional meander scanning pattern with 90° rotations between layers or a chessboard scanning pattern (5x5 mm^2 meander islands rotated 90° with respect to one another) with a 90° rotation between layers and a 1 mm by 1 mm lateral island shift between layers. The in-layer island overlap in the chessboard pattern was set at 0.0225 mm; the islands in each layer were scanned in a random order. Diagrams showing the two scanning patterns and the nominal bar dimensions are shown in Figure 1. For both scanning patterns, the two in-layer scanning directions were parallel and normal to the longitudinal direction of the bars, respectively (Figure 1); these will be referred to as scanning direction one (SD1) and scanning direction two (SD2), respectively. From here on, the scanning patterns will be referred to simply as 'bidirectional' and 'chessboard', respectively. All prints were performed with a power intensity of 225 W, a scanning speed of 2000 mm/s, a hatch spacing of 60 µm and a layer thickness of 30 µm.

Table 1: Nominal composition of the pre-alloyed gas atomised IN718 powder.

Element	Fe	Ni	Cr	Nb	Mo	Ti	Al	C
wt.%	Bal.	53	19	5.2	3.1	1.0	0.5	0.04

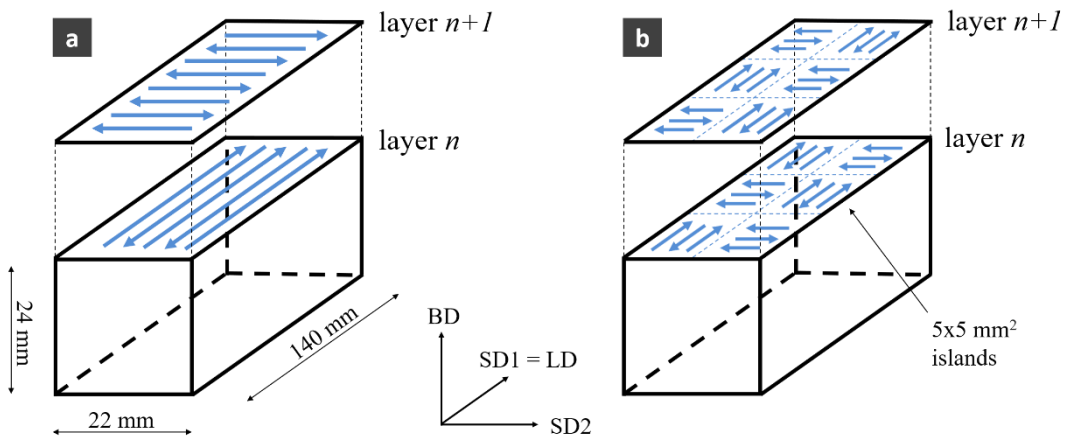


Figure 1: Diagrams showing the dimensions of the cuboidal bars and the laser scanning vectors (blue arrows) characteristic of the bidirectional (a) and chessboard (b) scanning strategies. The islands of the chessboard strategy have been enlarged for clarity. The building direction BD, the longitudinal scanning direction SD1 (coincident with the loading direction LD in tensile and fatigue tests) and the transversal scanning direction SD2 are also shown for reference.

The test pieces for monotonic and fatigue testing were machined from the cuboidal bars; the longitudinal direction of the test pieces coincided with that of the bars, thus the loading direction was parallel to SD1 and normal to both SD2 and the building direction (BD) in all tests performed in this work.

Tensile tests were carried out at room temperature in ambient atmosphere on cylindrical test pieces with a gauge diameter of 6 mm and a gauge length of 40 mm applying a strain rate of 2 $x10^{-4}$ s^{-1} using an Instron electromechanical testing system. Strain in the elastic regions was measured using a 12 mm extensometer; such extensometer was removed shortly after yield. Fully-reversed (R= -1) tension-compression fatigue tests were carried out at room temperature in ambient atmosphere on cylindrical test pieces with a gauge diameter of 5 mm, a gauge length of 16 mm and an average surface roughness R_a of 0.2 µm, imposing a 0.8% strain amplitude with a triangular waveform at a strain rate of 10^{-3} s^{-1} using an Instron servohydraulic fatigue testing system. Strain was measured with a 12 mm extensometer; loads and strains were recorded for all cycles in the tests. The tests were interrupted when the peak response stress in tension dropped by 50% with respect to that in the first cycle; as a result, the test pieces were not completely fractured when the tests were interrupted, although a large crack was clearly visible on each test piece. To preserve the part of the fracture surface formed during the test and

thereby enable the identification of the fatigue crack initiation site, the remaining ligament in each sample was cut using a precision slow saw to separate the two halves of each test piece.

Samples dedicated to the investigation of solidification microstructures in the as-built condition were taken ~10 mm from the edge of the bars; the bars were sectioned both normal and parallel to BD to enable the investigation of the anisotropic grain structures characteristic of LPBF alloys. The samples were mechanically ground using 800, 1200, 2000 and 4000 grit SiC abrasive paper, and then polished in a 50% solution of colloidal silica (0.04 μm) in distilled water. Such samples were subjected to secondary electron (SE) imaging and electron backscatter diffraction (EBSD) scans within a Zeiss Sigma 300 scanning electron microscope (SEM); SE imaging on polished samples was performed at 5 kV, whilst the EBSD scans were performed at 20 kV. The EBSD scans were carried out with a pixel size of 1 μm. EBSD data were then processed using the MTEX toolbox [37] within MATLAB to plot inverse pole figure (IPF) maps, as well as pole figures to investigate crystallographic textures. For optical microscopy, samples were etched with Kalling's reagent and a Nikon Eclipse ME600 microscope was used to acquire the images. Fractographic analyses after tensile and fatigue tests were carried out by SE imaging using a Zeiss Sigma 300 SEM operating at 20 kV.

Thin foils for transmission electron microscopy (TEM) were prepared by twin-jet electropolishing in a solution of 10 % perchloric acid in methanol applying 20 kV at -5 °C with a Struers TenuPol-5. Foils dedicated to the investigation of the as-built microstructure were taken ~10 mm from the edge of the bars; in turn, foils dedicated to the investigation of the alloy's microstructure after tensile and fatigue testing were taken from the gauge section of the respective test pieces. TEM and scanning TEM (STEM) investigations were carried out using a Jeol JEM-2100F microscope operating at 200 kV. Most TEM micrographs in this work were obtained in two-beam conditions; the relevant diffraction patterns and diffraction vectors are shown on each micrograph. Energy-dispersive X-ray spectroscopy (EDX) analysis was performed within STEM using an Oxford Instruments detector. Elemental maps were processed using MATLAB; in particular, to limit any bias arising from varying signal quality within the map, the counts for each element at each pixel were normalised with the total number of elemental counts for that pixel. Hence, the EDX maps are coloured according to each element's percentage count fraction at each pixel.

For atom probe tomography (APT), blanks with dimensions of 0.5x0.5x22 mm^3 were cut normal to BD and electropolished following standard procedures [38]. Experiments were performed in a CAMECA local electrode atom probe (LEAP) 4000X Si in laser-assisted acquisition. With a detector efficiency of 57% and flight path length of 90 mm, experiment parameters were set to temperature of 50 K, pulse rate of 200 kHz, laser energy of 50 pJ, and detection rate of 1.0%. The software AP Suite 6.1 was used for reconstructing and analysing the datasets. Standard reconstruction parameters were used, i.e., image compression faction of 1.65 and k-factor of 3.3. Proximity histograms (proxigrams) were obtained for a total length of 4 nm, with a step size of 0.1 nm.

X-ray computed tomography (XCT) scans were carried out to investigate the porosity within the gauge section of the fatigue test pieces prior to testing. Such scans were carried out at 210 kV with a power of 10 W and an exposure time of 1 s. A 1 mm layer of tin was used for filtration, and 8-frame averaging was used to minimise noise in the data. An isotropic voxel size of 5 µm was achieved for each sample. XCT data was analysed using ImageJ. A threshold was applied to each slice to separate the pores from the consolidated material, allowing the calculation of the porosity fraction across the gauge section of the test pieces. Finally, the porosity in each test piece was reconstructed using the 3D viewer within Fiji.

3 RESULTS

3.1 AS-BUILT MICROSTRUCTURE

EBSD scans were carried out on samples fabricated using the two scanning patterns; each sample was sectioned both normal to BD (top view) and to SD1 (side view), and an EBSD scan was performed on each section. The resulting IPF maps with respect to the BD are shown in Figure 2.

The top view EBSD map of the bidirectional sample (Figure 2a) shows that the grain structure reflected the path of the laser beam in the two in-layer orthogonal scanning directions, with very fine grains arranged in a regular grid and larger grains in between (Figure 2a). Similar features have been previously reported in LPBF IN718 [15,16]. Similarly, the associated side view EBSD map (Figure 2b)

showed regularly-spaced slender columnar grains extending along the building direction separated by more equiaxed grains. The consistent regular spacing indicates that the fine grains observed in the top view (Figure 2a) were the slender columnar grains in the side view (Figure 2b). The regular spacing of ~60 μm (equal to the hatch spacing in this work) related to the fact that such grains formed along the centreline of each scanning track (as thoroughly discussed in [31,32]), where the local thermal gradient was parallel to BD, which is consistent with their <100> orientation parallel to BD. Their columnar morphology (Figure 2b) originated from epitaxial growth across several deposition layers during fabrication thanks to the regular stacking of melt pools inherent to the bidirectional scanning strategy. The larger grains seen in the top view EBSD map (Figure 2a) formed on the sides of each scanning track, where the thermal gradient is inclined with respect to BD; such misalignment made epitaxial growth across layers less favourable for these grains, leading to the more equiaxed morphologies seen in the side view (Figure 2b). The formation of this grain structure in fcc alloys processed by LPBF has been explained in greater detail elsewhere [31,32].

The top view EBSD map of the chessboard sample (Figure 2c) appeared rather similar to that of the bidirectional sample (Figure 2a), as the path of the laser beam within each 5x5 mm^2 island was analogous to that in the bidirectional pattern. However, despite the analogous scanning vectors and thus melt pool stacking, the side view map of the chessboard sample (Figure 2d) revealed a significantly less ordered grain structure compared to that of the bidirectional sample (Figure 2b). This related to the fact that the shorter scanning lines within each island in the chessboard pattern led to a higher local substrate temperature and thereby induced deeper melt pools (compare Figure 2e and f). The distinct melt pool morphologies associated with the two scanning patterns led to different grain growth conditions and thereby different grain morphologies. Such distinct grain growth conditions also led to differences in the average grain sizes measured from side view EBSD maps, which were 13.9 μm and 15.4 μm for the bidirectional and chessboard sample, respectively. In contrast, the average grain sizes measured in the top views of the two samples (Figure 2a and c) were very similar at 11.4 and 11.6 μm, respectively. It is noted, however, that there was great variability in grain size within each map; the grain size distributions obtained from each EBSD map are shown in the Appendix (Figure A.1).

To analyse the texture developed in the builds, pole figures generated using the data from the top view maps of the two samples (Figure 2a and c) are shown in Figure 2g and h. Both samples exhibited very similar weak cube textures, with <100> crystallographic orientations aligned preferentially along the two scanning directions and the building direction; this is consistent with reports in the literature for similar scanning patterns [31].

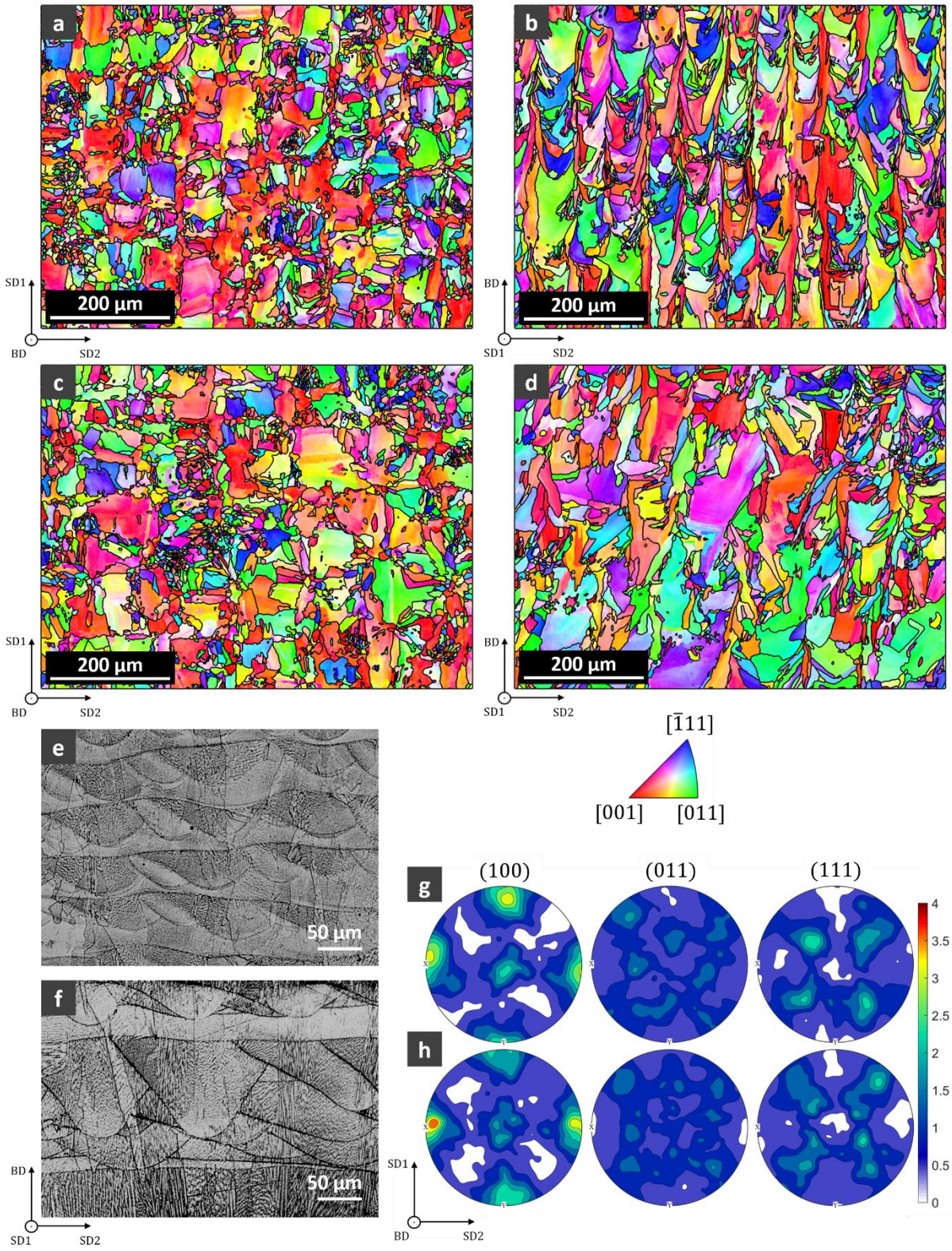


Figure 2: EBSD IPF-BD maps of the bidirectional (a, b) and chessboard (c, d) samples. Optical microscope micrographs showing melt pool morphologies after etching in the bidirectional (e) and chessboard (f) samples. Pole figures generated using the top-view EBSD data for the bidirectional (g) and chessboard (h) samples. The building and scanning directions are indicated in the bottom left corner of each image for reference.

Low-magnification SEM micrographs of the bidirectional sample (Figure 3a) confirmed the ordered grain structure observed in the side view EBSD map (Figure 2b). Higher-magnification micrographs further showed that both the slender columnar grains (Figure 3b) and the more equiaxed grains between them (Figure 3c) were composed of very fine solidification cells, which are shown in greater detail in Figure 3d. Similarly, the less ordered yet columnar grain structure observed in the chessboard sample (Figure 3e) was consistent with that revealed by EBSD (Figure 2d); in addition, the chessboard sample exhibited a fine solidification cellular microstructure (Figure 3f) analogous to that seen in the unidirectional sample (Figure 3d). Fine solidification cells have been widely reported for both IN718 and other face-centred cubic (fcc) alloys fabricated by LPBF and relate to the high cooling rates characteristic of this fabrication method [8,9,35,39,40]. The average cell spacings were measured from a number of micrographs using ImageJ and were found to be 0.43 ± 0.08 and 0.50 ± 0.11 μm for the bidirectional and chessboard sample, respectively. The slightly larger average cell size in the chessboard sample related to the higher local substrate temperature (and thus lower cooling rates) associated with the shorter scanning lines within each island. The cooling rate ε during fabrication of the two samples can be estimated using their cell spacing δ expressed in μm according to [12,41]:

$$\delta = 80\varepsilon^{-0.33}$$

The measured cell spacings yielded cooling rates of ~7.5 x10^6 °C/s and ~4.8 x10^6 °C/s for the bidirectional and chessboard samples, respectively. Finally, several fine particles were observed at the cell boundaries in both samples (Figure 3d and f).

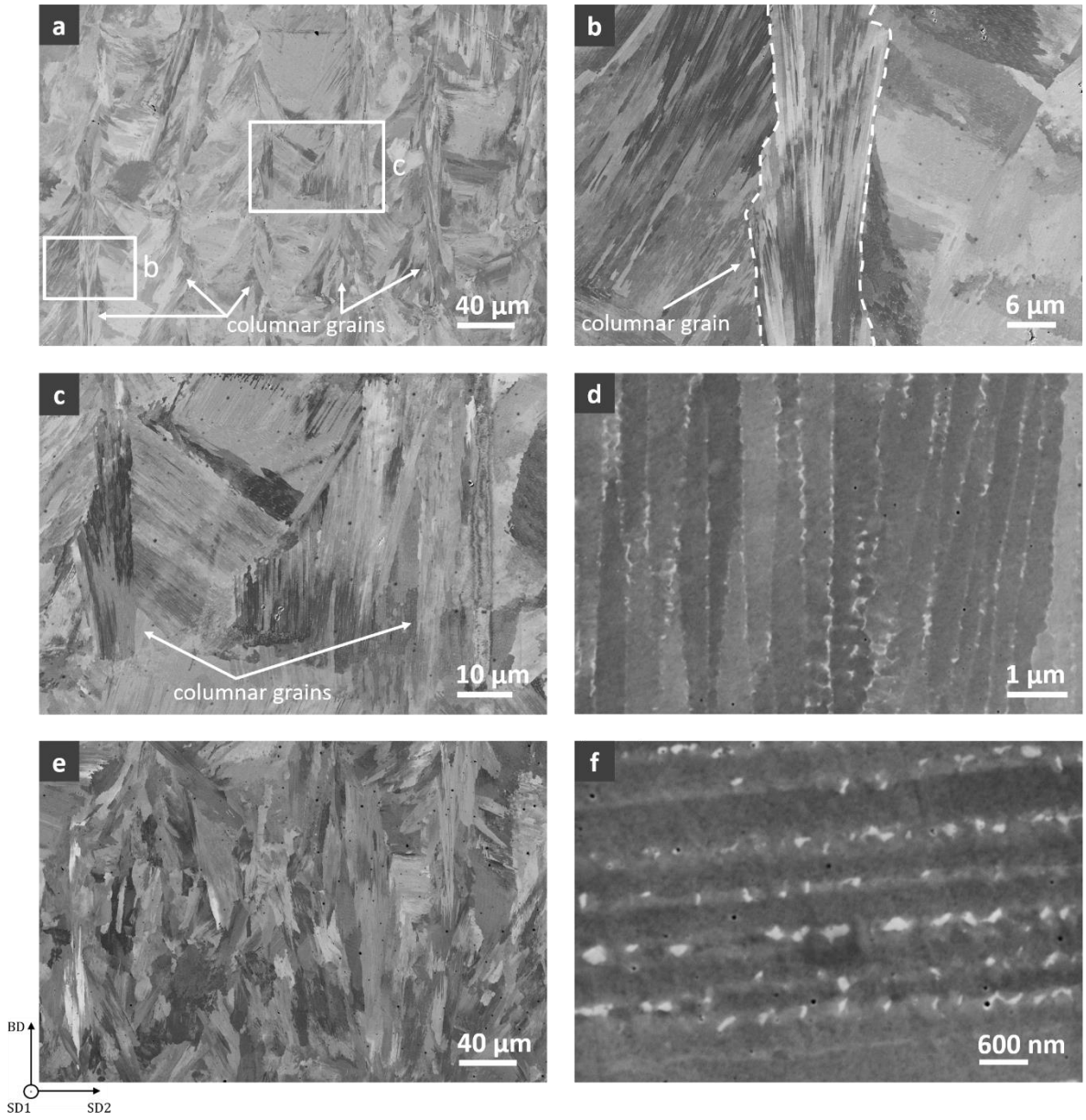


Figure 3: SEM micrographs showing the microstructure of a bidirectional sample (a, b, c, d) and a chessboard sample (e, f). The white rectangles in (a) indicate the locations of micrographs (b) and (c). The reference coordinate system is common to all micrographs and is shown in the bottom left corner of (e).

The alloy's as-built microstructure was further investigated by TEM; micrographs from a bidirectional sample are shown in Figure 4. Dislocation contrast was deliberately avoided in Figure 4a and b to enable a clearer observation of the solidification cellular structure and of the rather homogeneous distribution of fine particles at cell boundaries. In turn, micrographs obtained in two-beam conditions (Figure 4c and d) revealed high dislocation densities at cell boundaries, with lower yet considerable dislocation

densities within the cell interiors. High dislocation densities in as-built LPBF alloys are widely reported and relate to rapid solidification and the associated severe thermal stresses during printing [10,11,30,35,39].

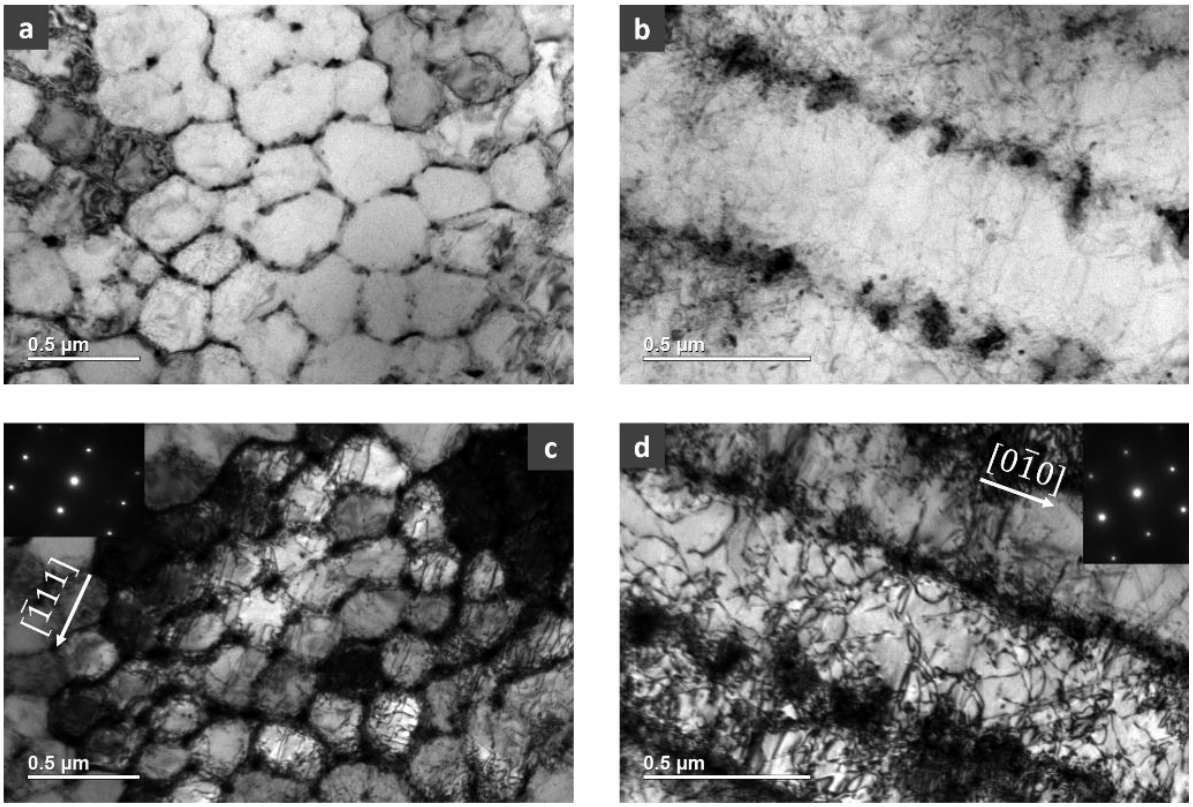


Figure 4: TEM-BF micrographs showing the microstructure of the as-built bidirectional sample. Image (a) and (b) were obtained by avoiding dislocation contrast. Image (c) was obtained with $\boldsymbol{B}=[1\bar{1}2]$ *and* $\boldsymbol{g}=[\bar{1}11]$*, while image (d) was obtained with* $\boldsymbol{B}=[101]$ *and* $\boldsymbol{g}=[0\bar{1}0]$*. The foil normal was parallel to SD1 for all micrographs; BD and SD2 were contained in the plane of the foil.*

The particles at cell boundaries were investigated by means of both APT and STEM-EDX to determine their chemical composition. APT analysis revealed the presence of two distinct phases at cell boundaries; Figure 5a-c show the reconstructed volume of an APT dataset where these two phases are delineated by concentration isovalues of Nb (17.40 at.%, Figure 5a and b) and C (16.95 at.%, Figure 5c), respectively, following the method proposed by Theska *et al.* [42]. Figure 5a and b show two views of the same particle, whilst Figure 5c shows a number of fine particles within the larger one. The

chemical compositions of the two phases obtained from the same APT dataset are shown in Table 2 together with that of the matrix. The larger particle exhibited a significant enrichment in Nb, a slight enrichment in Ti and Mo, and a depletion in Ni, Fe and Cr compared to the matrix (Table 2). Its chemical composition was consistent with that of the Laves phase, which has been often reported to form at cell boundaries in as-built LPBF IN718 due to the segregation of heavy elements such as Nb, Ti and Mo during solidification [7,9,10,12,23,27]. In turn, the finer particles were identified as carbides by virtue of their high concentration of C (Table 2). Proxigrams showing the variation in elemental composition across the matrix/Laves interface and across the matrix/carbide interface are shown in the Appendix (Figure A.2). To investigate whether APT results were representative of all particles at cell boundaries, STEM-EDX elemental mapping was carried out in a region containing a number of particles (Figure 5d). STEM-EDX results showed that all particles in the region investigated were characterised by an enrichment of Nb, Ti and Mo and a depletion of Ni, Fe and Cr compared to the matrix, thus confirming that the particles decorating the cell boundaries were mainly Laves particles. STEM-EDX results also showed that significant C enrichment was only detected in some of the particles in the region investigated (Figure 5d); this shows that the fine carbides detected by APT (Figure 5c) were not always present within Laves particles. Finally, Figure 5d shows some C enrichment also within cell interiors, indicating that some very fine carbides, barely visible in the STEM micrograph, were present in such regions; this is supported by the fact that depletions of Ni, Fe and Cr characteristic of carbides (Table 2) were observed at the same locations. It should be noted that the TEM, STEM-EDX and APT investigations shown in Figure 4 and Figure 5 were performed on a bidirectional sample; however, analogous results (not shown here) were found in a chessboard sample.

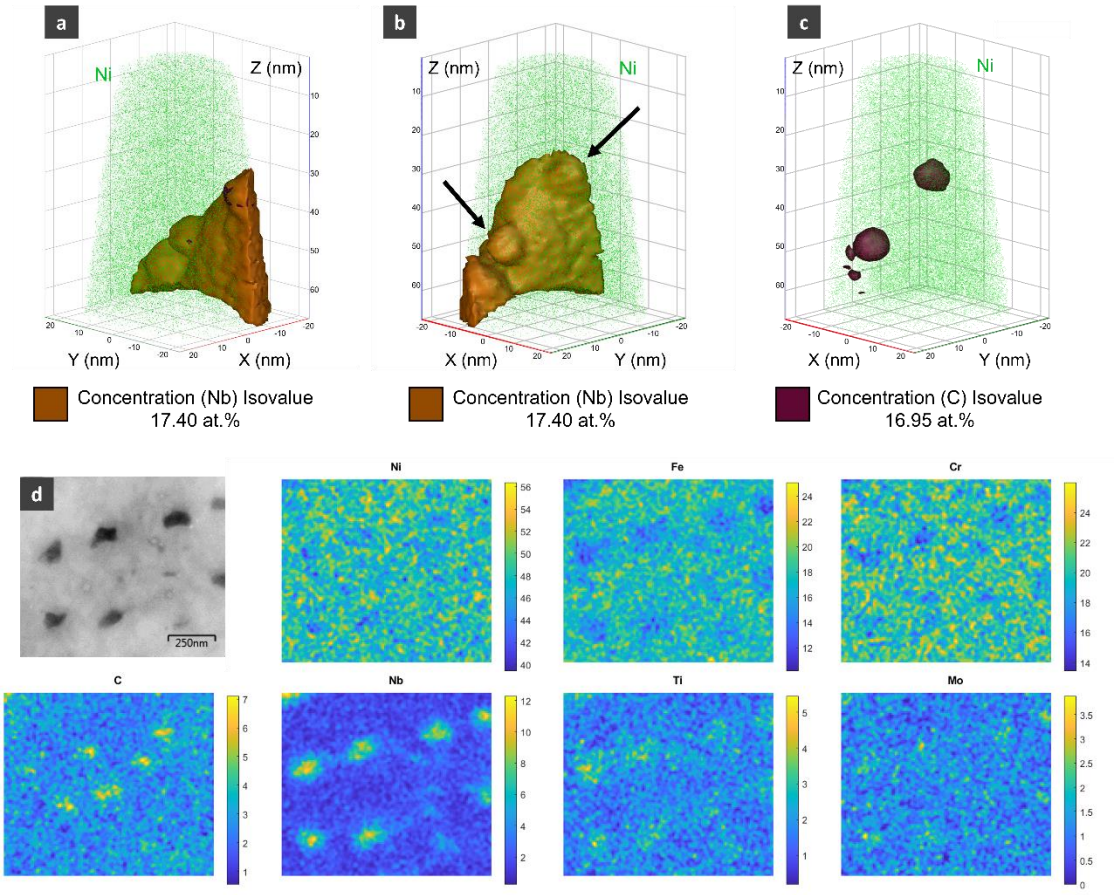


Figure 5: Reconstructed volume of an APT dataset where a Laves particle (a, b) and a number of fine carbides within such particle (c) are delineated by concentration isovalues of Nb (17.40 at.%) and C (16.95 at.%), respectively. The locations of the two largest carbides are indicated by black arrows in (b), whilst the green dots indicate Ni atoms. A STEM micrograph and the associated STEM-EDX elemental maps of a number of fine particles at cell boundaries are shown in (d). Each pixel in the maps is coloured according to each element's percentage count fraction at that location. Both APT and STEM-EDX analyses were performed on a bidirectional sample.

Table 2: Chemical compositions (at.%) of matrix, Laves particle and carbides shown in Figure 5a-c obtained via APT on a bidirectional sample in the as-built condition.

	Ni	Fe	Cr	Nb	Mo	Ti	Al	C
Matrix	52.30 ± 0.06	17.42 ± 0.03	20.57 ± 0.03	5.43 ± 0.02	1.60 ± 0.01	1.45 ± 0.01	0.92 ± 0.01	0.05 ± 0.001
Laves	39.79 ± 0.14	11.89 ± 0.07	16.23 ± 0.08	21.21 ± 0.10	4.33 ± 0.04	3.66 ± 0.04	0.45 ± 0.01	1.73 ± 0.03
Carbides	5.15 ± 0.38	0.85 ± 0.15	7.85 ± 0.48	29.09 ± 1.01	8.37 ± 0.50	15.40 ± 0.70	0.14 ± 0.06	30.89 ± 1.05

3.2 MONOTONIC TENSILE TESTS

Uniaxial monotonic tensile tests were conducted on the bidirectional and chessboard samples at room temperature. The resulting engineering stress/strain curves are shown in Figure 6. Relevant tensile properties measured in these tests are shown in Table 3, together with the minimum tensile properties defined by the ASTM standard for stress relieved additively manufactured IN718 [43] and the tensile properties reported in a previous study on horizontally-built LPBF IN718 in the as-printed condition [22], included for reference. The bidirectional sample exhibited higher elastic modulus E, yield stress at 0.2% offset σ_y, ultimate tensile strength σ_u and elongation to fracture ε_f compared to the chessboard sample (Table 3). The tensile properties of the two samples were otherwise similar to those reported in the literature [22] and higher than the minimum values defined by the ASTM standard [43], with the exception of the elongation to fracture (Table 3); this likely related to the large porosity fractions in the builds in this work, as will be shown later. The tensile curves of the two samples, in terms of both yielding and strain hardening, were analogous to one another (Figure 6), and very similar to those reported in the literature for IN718 fabricated by LPBF in the as-built condition [16,22,28,34]. It should be noted that the slight stress drop observed for both samples shortly after yield (inset of Figure 6) was due to a brief interruption of the test for extensometer removal and was therefore not related to the material's response to uniaxial straining. Table 3 also includes the tensile properties of a bidirectional and a chessboard sample after a standard heat treatment (960 °C/1 h + air cooling, 720 °C/8 h + 620 °C/9.5 h + air cooling) that is known to promote the precipitation of fine γ' and γ'' precipitates [10] for reference. These samples were from the same batch as the as-built ones and were tested in analogous conditions. The significantly increased yield stresses and ultimate tensile strengths of heat treated samples highlight the key contribution of strengthening precipitates; however, the poor elongation to fracture shows their detrimental effect on the alloy's ductility, in agreement with reports in the literature [9,10,23]. It should be noted that the properties shown in Table 3 for both as-built and heat treated

samples were extracted from four individual tensile tests (one for each condition); the reported uncertainties related to the identification of the most linear parts of the curves within the elastic regimes (inset of Figure 6) and to the consequent uncertainties in the determination of elastic moduli, yield stresses and yield strains.

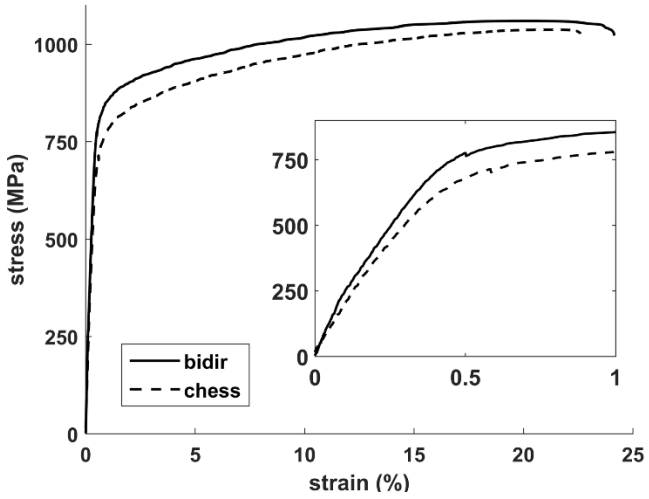


Figure 6: Engineering stress/strain curves for the as-built bidirectional and chessboard samples in during monotonic tensile loading at room temperature. The inset shows the elastic region and the yielding behaviour of both samples in greater detail.

Table 3: Tensile properties of the as-built bidirectional and chessboard samples extracted from the curves shown in Figure 6. The minimum tensile properties defined by the ASTM standard for stress relieved additively manufactured IN718 [43] *and those reported in another study of horizontally-built LPBF IN718 in the as-printed condition* [22] *are included for reference. The tensile properties of bidirectional and chessboard samples from the same batch tested with the same conditions after a common heat treatment (HT) are also included for reference.*

	E (GPa)	σ_y (MPa)	ε_y (%)	σ_u (MPa)	ε_f (%)
bidirectional	213 ± 23	794 ± 12	0.58 ± 0.04	1060	24.2
chessboard	189 ± 16	709 ± 11	0.58 ± 0.03	1038	22.6
Sabelkin *et al.* [22]	89 ± 2	602 ± 18	-	986 ± 26	20 ± 1
ASTM standard [43]	-	635	-	980	27
bidirectional HT	210 ± 9	1253 ± 9	0.80 ± 0.03	1495	7.9
chessboard HT	153 ± 5	1090 ± 6	0.91 ± 0.03	1173	1.57

The fracture surfaces of the as-built bidirectional and chessboard samples after tensile testing are shown in Figure 7a and b, respectively. Both samples exhibited cracking along linear features; the regular spacing between such features (Figure 7c) suggest that they coincided with the interfaces between deposition layers (as BD was normal to the loading direction LD). In other words, such regularly-spaced cracks were generated by layer de-bonding during the tensile tests. In addition, large defects such as lack-of-fusion pores were apparent on the fracture surfaces (Figure 7d).

TEM-BF micrographs of the bidirectional sample after tensile testing are shown in Figure 8. Both micrographs show that the solidification cellular structure was retained during testing, together with the high dislocation densities at cell boundaries. However, the large plastic strains in tension resulted in an increase in dislocation density within cell interiors (Figure 8).

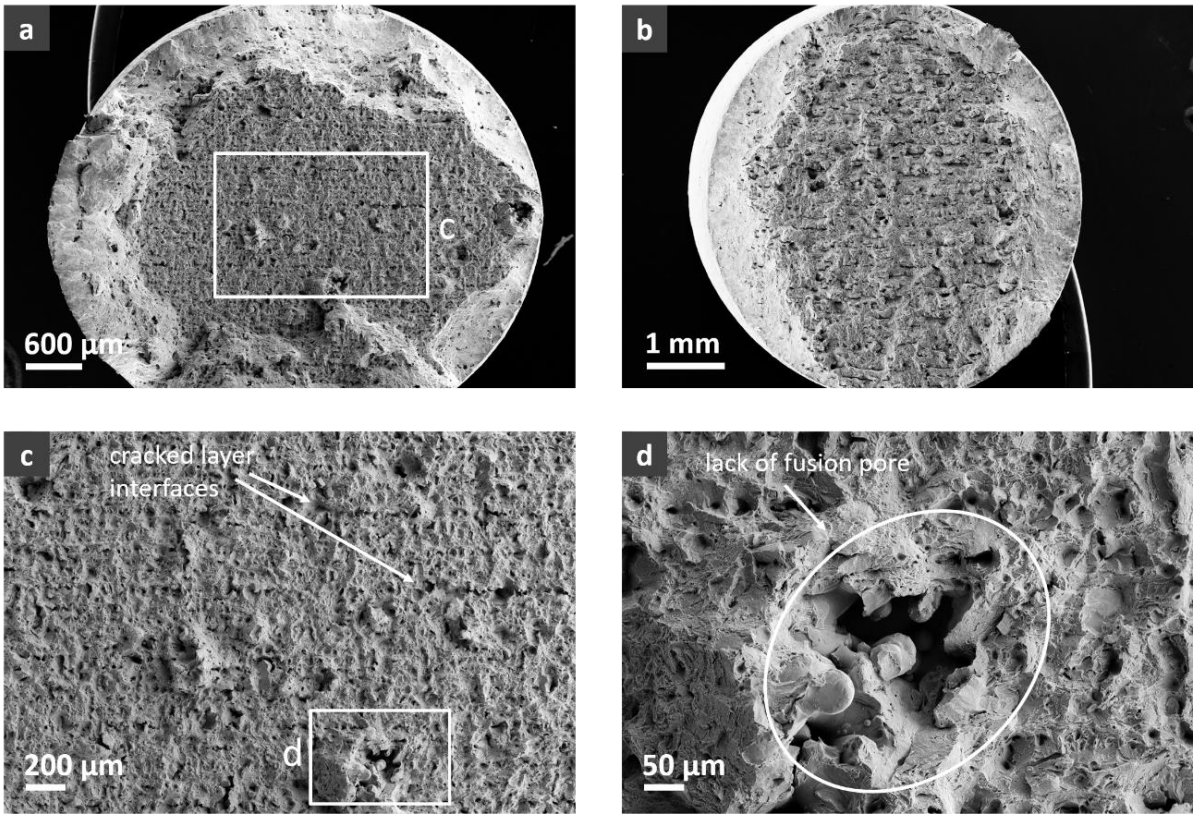


Figure 7: SEM micrographs of the fracture surfaces of the as-built bidirectional (a, c, d) and chessboard (b) samples after monotonic tensile testing at room temperature. The white rectangles in (a) and (c) indicate the locations shown in the other higher-magnification micrographs.

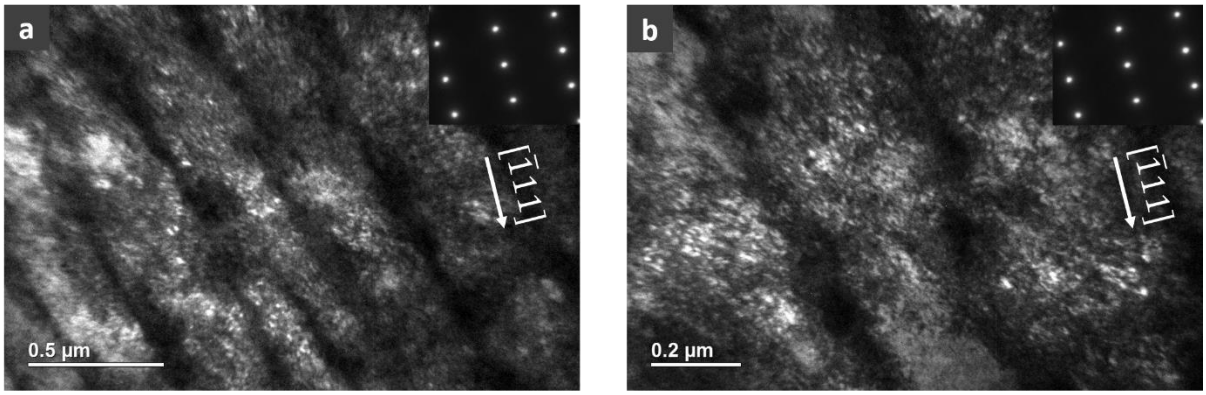


Figure 8: TEM-BF micrographs of the as-built bidirectional sample after monotonic tensile testing at room temperature. Both images were obtained with $\boldsymbol{B}=[\bar{1}1\bar{2}]$ *and* $\boldsymbol{g}=[\bar{1}11]$*. The foil normal was parallel to the loading direction and thus to SD1 for both micrographs; BD and SD2 were contained in the plane of the foil.*

EBSD scans were performed on the specimens' cross sections, just below the fracture surface, to investigate microstructural evolution after tensile testing; the resulting maps, coloured according to the inverse pole figure with respect to the loading direction (LD) are shown in Figure 9. The microstructure of both samples appears significantly different from that observed in samples in the as-built condition (Figure 2a-d) due to the large strains experienced. This is apparent when comparing the pole figures for the bidirectional sample after testing (Figure 9c) with those in the as-built condition (Figure 2g; the different coordinate systems should be kept in mind when comparing such pole figures). The <100> texture along SD1, which was parallel to the loading direction LD, increased during tensile testing; in turn, the <100> textures along BD and SD2 decreased. In addition, some <111> texture developed in the loading direction in the tested sample, in contrast with the as-built sample. This shows that the large strains experienced by the test pieces during the monotonic tensile tests induced significant grain rotation. The generation of <111> texture along LD indicates that, as expected, deformation occurred via slip on {111} planes [39,44].

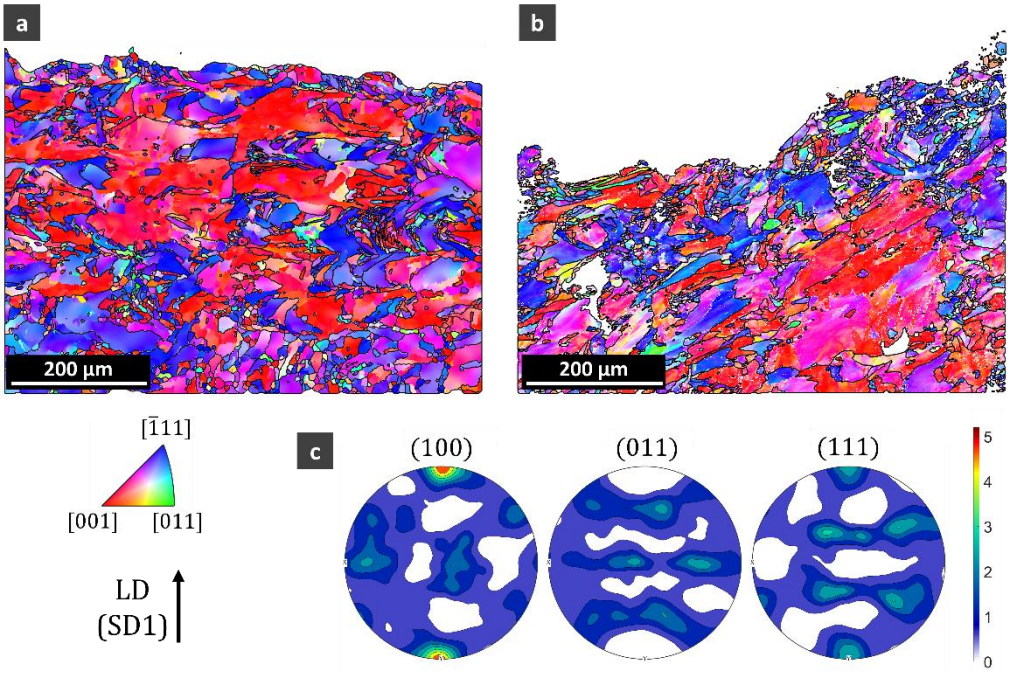


Figure 9: EBSD IPF-LD maps of the cross sections of the bidirectional (a) and chessboard (b) samples after monotonic tensile loading at room temperature. These EBSD scans were performed in the regions right below the fracture surfaces, which are visible at the top of each image. Pole figures generated with the data in (a) for the bidirectional sample are shown in (c). The loading direction LD (parallel to SD1) is indicated for reference.

3.3 FATIGUE TESTS

XCT scans were performed on the fatigue specimens prior to testing. Volumetric reconstructions of the porosity within the two test pieces are shown in Figure 10a and b. The chessboard sample was significantly more porous than the bidirectional one, exhibiting a porosity fraction of 1.62% compared to 0.31% in the bidirectional sample. Figure 10c and d show the variation in porosity fraction along the gauge length in the bidirectional and chessboard test pieces, respectively. The porosity content of the bidirectional test piece was found to increase slightly along the gauge length (Figure 10c). In turn, the porosity fraction varied in a very peculiar way along the gauge length of the chessboard test piece, with very high peaks occurring at regular intervals of ~1 mm (Figure 10d).

To investigate pore morphologies and distribution in the two samples, the XCT slices with the highest porosity fraction in the bidirectional and chessboard test pieces are shown in Figure 10e and f,

respectively. The majority of pores in both samples were found to be rather large and characterised by sharp and irregular shapes, suggesting that they formed as a consequence of lack-of-fusion. In addition, whilst the pore distribution in the bidirectional sample did not appear to follow any particular pattern (Figure 10e), pores in the chessboard test piece were clearly aligned predominantly along two orthogonal directions (Figure 10f). The pores elongated along SD2 likely formed due to poor bonding between layers during fabrication. The more equiaxed pores, in turn, were arranged in columns along BD with a regular spacing of ~1 mm (Figure 10f), and exhibited morphologies commonly associated with lack-of-fusion. Such regular spacing suggests that these pores were related to the 1 mm shift between islands in subsequent layers; this is supported by similar features reported in another Ni-based superalloy printed with an analogous scanning pattern [45]. The relatively high porosity fractions in the test pieces of study, particularly in the chessboard sample, were likely associated with the fact that the process parameters used for the prints were not optimised specifically for the powder used. In particular, the spreading of the powder was found to not be optimal during fabrication; this likely related to the shape and size distribution of the powder particles. It is noted that the XCT slice shown in Figure 10f for the chessboard sample coincided with one of the porosity fraction peaks seen in Figure 10d; the porosity characteristics within the XCT slices corresponding to the other porosity fraction peaks in this sample were found to be analogous to those shown in Figure 10f.

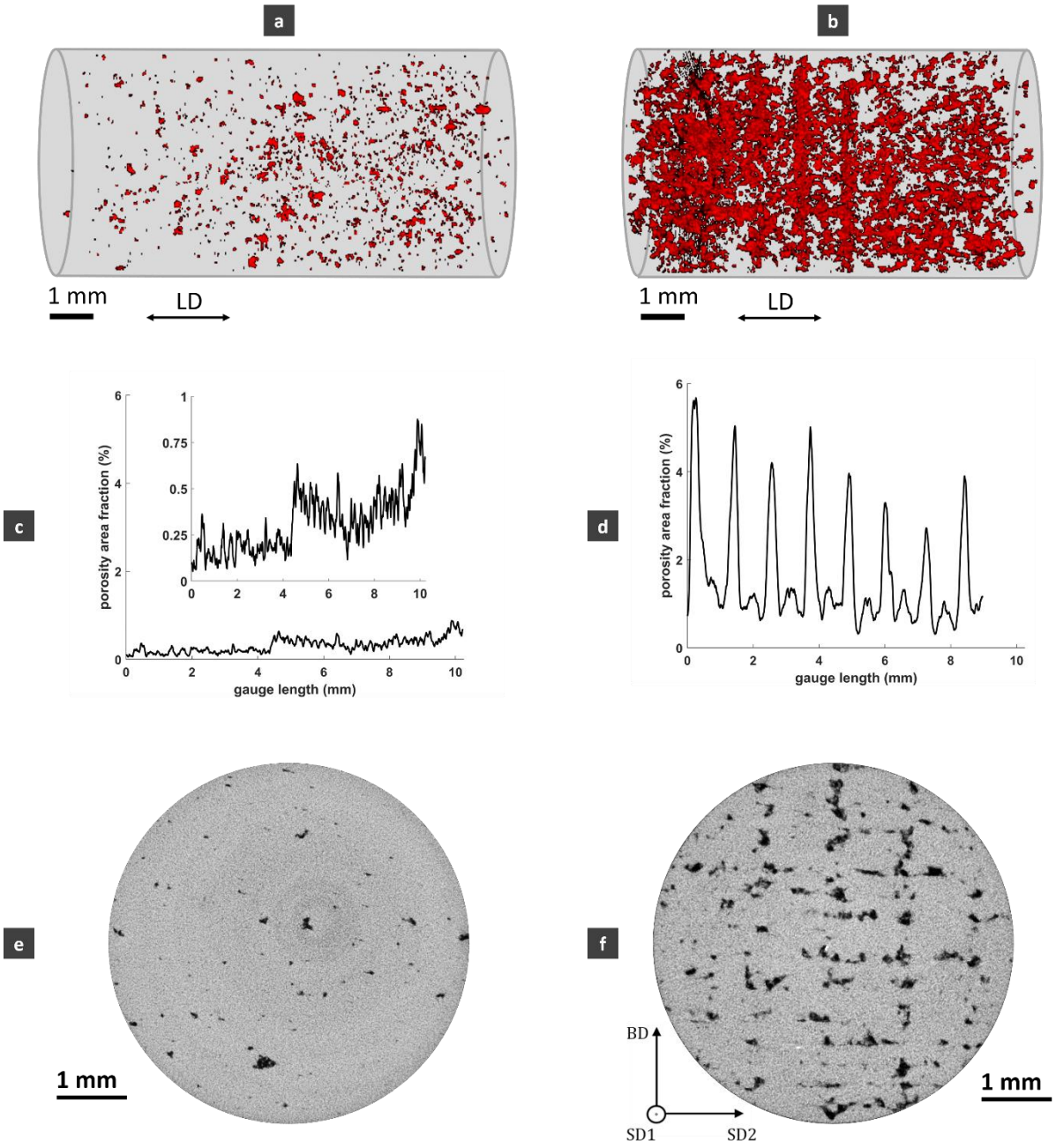


Figure 10: Volumetric reconstruction of the porosity within the bidirectional (a) and the chessboard (b) fatigue test pieces prior to testing from XCT data. The variation in porosity area fraction along the gauge length of the two test pieces is shown in (c) and (d). The XCT slices characterised by the highest porosity content in the bidirectional and chessboard fatigue test pieces are shown in (e) and (f), respectively.

Stress and strain data for the first and half-life cycles of the bidirectional and chessboard test pieces are shown in Figure 11a and b, respectively. The first-cycle loops of the two samples exhibited qualitatively

analogous shapes, indicating a very similar mechanical response. However, the elastic modulus, yield strength and peak response stress were seen to be higher in the bidirectional sample in both tension and compression. These results are in agreement with those of the monotonic tensile tests (Figure 6 and Table 3).

The shape of the stress/strain loops qualitatively did not change significantly at half-life, closely resembling that for the first cycles of both samples (Figure 11a and b), indicating a rather stable cyclic response. The evolution of maximum and minimum response stresses during cyclic loading are shown in Figure 11c. This image shows that the bidirectional sample exhibited a significantly longer fatigue life (610 cycles) compared to the chessboard sample (197 cycles), which correlates well with its higher degree of consolidation (Figure 10) and with its greater ductility in the monotonic tensile tests (Figure 6). The behaviour of the two samples was, once again, rather similar; both samples exhibited pronounced cyclic hardening in the first ~20 cycles, followed by moderate but continuous cyclic softening until failure. The evolution of the plastic strain range throughout the fatigue tests, calculated for each loading cycle as the strain range at zero stress, is shown in Figure 11d. The plastic strain range of both samples decreased rapidly in the first 20 cycles, then gradually increased until failure; this behaviour related closely to the cyclic hardening and softening phases shown in Figure 11c. However, Figure 11d also shows that the chessboard sample consistently experienced larger plastic strain ranges compared to the bidirectional sample; this was a consequence of the lower yield stress of the chessboard sample (Table 3).

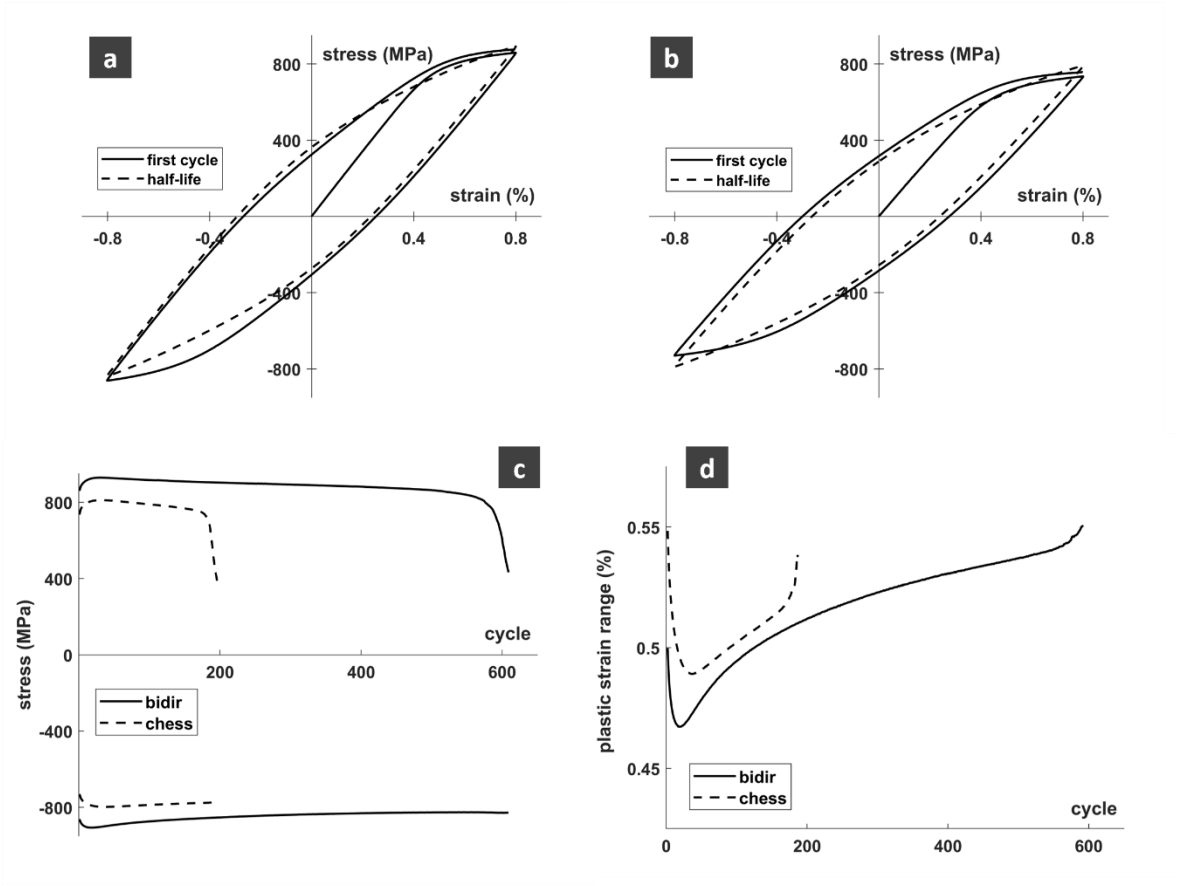


Figure 11: Stress/strain data for the first and the half-life cycles for the bidirectional sample (a) and the chessboard sample (b) in the as-built condition. The variation of maximum and minimum stresses throughout the fatigue tests for both samples is shown in (c). The variation of plastic strain range is shown in (d).

SEM micrographs of the fracture surfaces of the bidirectional and chessboard specimens after fatigue testing at room temperature are shown in Figure 12 and Figure 13, respectively. Fatigue crack initiation occurred at a number of large pores located close to the surface in the bidirectional sample (Figure 12a and b), as confirmed by the numerous fatigue striations found in their vicinity (e.g., Figure 12c), in agreement with what is reported in the literature for LPBF IN718 [13,15,21,23]. The shape of the initiating pores and the unmelted powder particles seen within them (e.g., Figure 12b) confirmed that these defects were lack-of-fusion pores, supporting the observations made earlier (Figure 10). The numerous initiation sites indicate that crack initiation occurred rather rapidly, likely as a consequence of the considerable bulk plasticity coupled with the large pore sizes. Finally, in very few regions evidence of fracture at the interfaces between layers could be seen on the fracture surface (Figure 12d),

which was similar (though significantly less marked) to what was seen after monotonic loading (Figure 7a and b). Layer de-bonding during cyclic loading had previously been reported for LPBF IN718 [22].

Large sub-surface pores were also seen to initiate cracks in the chessboard sample (Figure 13a and b); here, the pores were found to be larger than the ones seen in the bidirectional samples, as well as more numerous. These observations are consistent with the XCT results (Figure 10). Cracks were found to initiate also at the interfaces between layers (Figure 13a and c), as confirmed by the several fatigue striations emanating from them (Figure 13d), in a similar way to that observed in the bidirectional sample (Figure 12d). Here, however, cracking at the layer interfaces was significantly more marked in terms of both number and length of interface cracks (white dashed lines in Figure 13a), which is consistent with XCT data (Figure 10f). In fact, a careful observation of the fracture surface of the chessboard sample (Figure 13a) reveals that the large lack-of-fusion pores (e.g., Figure 13b) were elongated in a direction normal to that of the cracked layer interfaces. This arrangement closely resembled that seen in the XCT slice shown in Figure 10f, thus indicating that fatigue fracture likely occurred in a region characterised by one of the porosity peaks shown in Figure 10d.

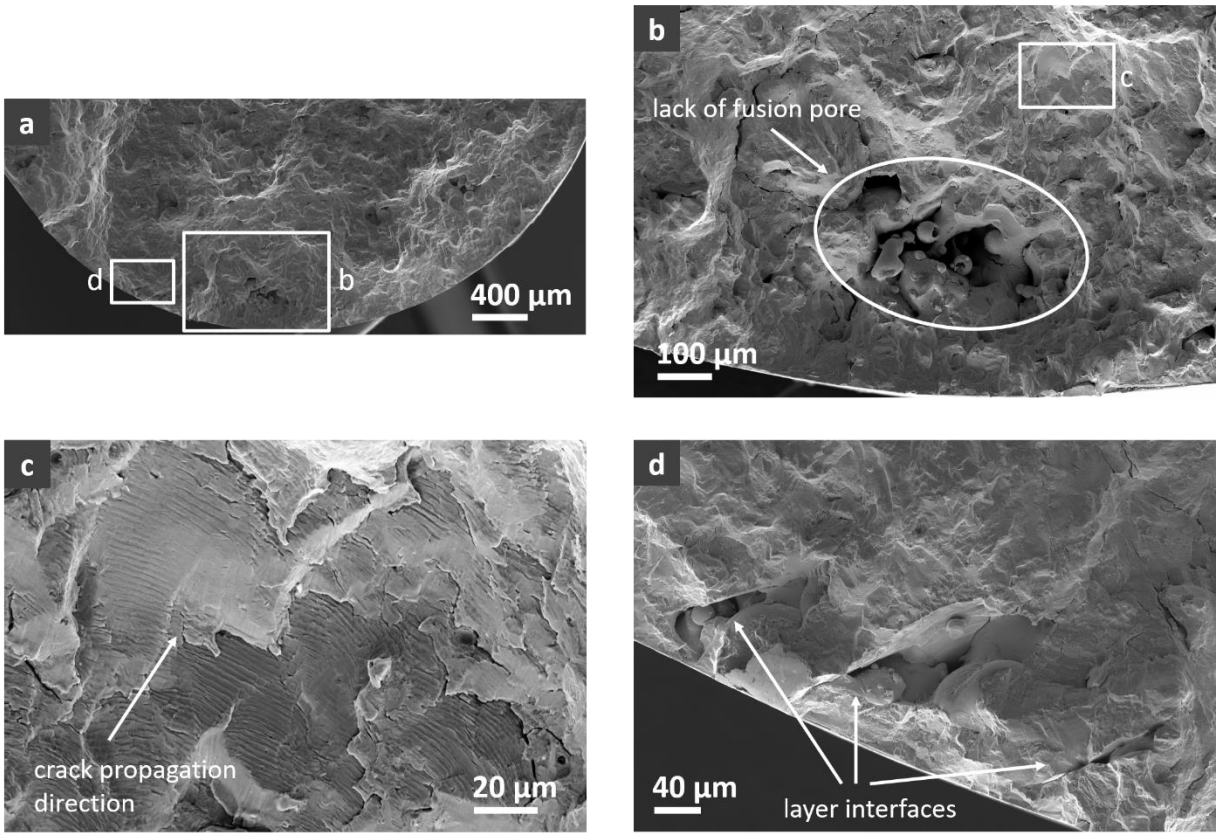


Figure 12: SEM micrographs of the fracture surface of the bidirectional sample subjected to fatigue testing at room temperature. The white rectangles in (a) and (b) indicate the locations shown in the other higher-magnification micrographs.

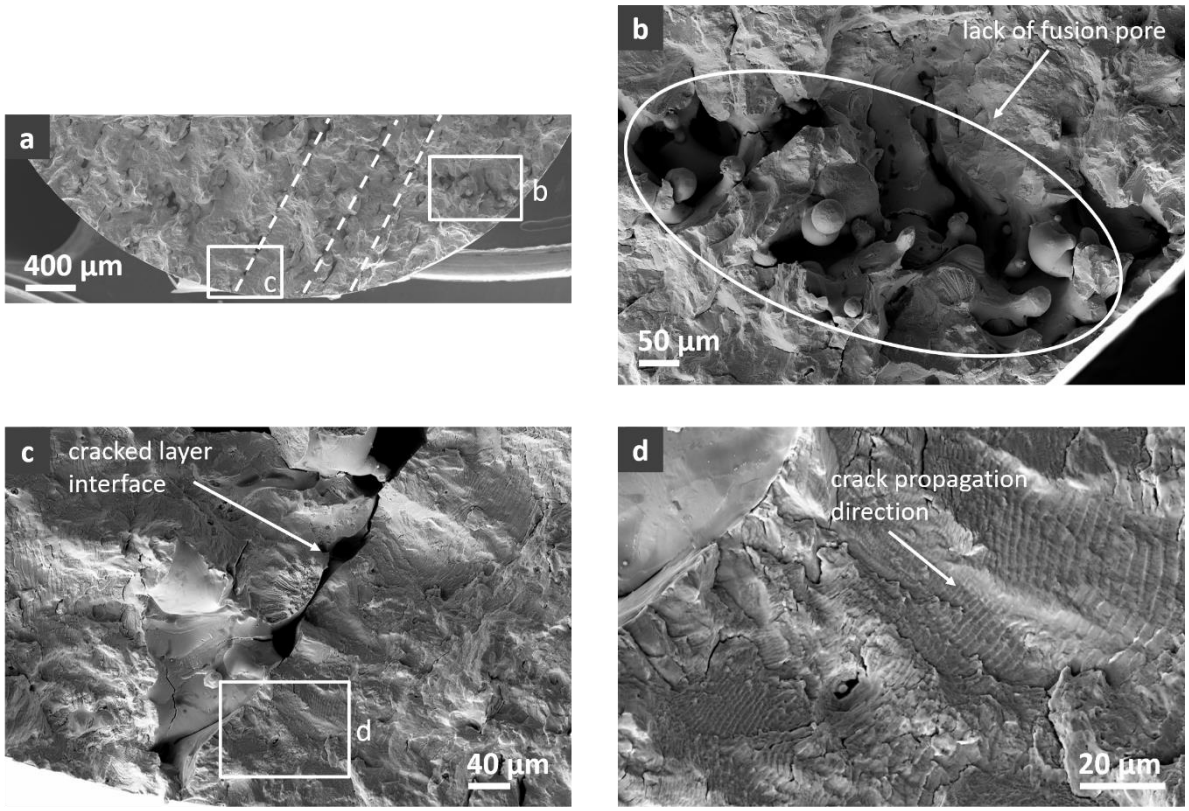


Figure 13: SEM micrographs of the fracture surface of the chessboard sample subjected to fatigue testing at room temperature. The white rectangles in (a) and (c) indicate the locations shown in the other higher-magnification micrographs. The white dashed lines in (a) indicate cracked layer interfaces.

TEM-BF micrographs of the bidirectional specimen after fatigue testing at room temperature are shown in Figure 14. In many regards, the microstructure appeared similar to that in the as-built condition (Figure 4c and d); in particular, the cellular microstructure was retained, together with the high dislocation densities at cell boundaries and several dislocations within cell interiors (Figure 14a and b). The dislocation density within cells appeared to be qualitatively higher compared to that in the as-built sample (Figure 4c and d), yet lower compared to that after monotonic tension (Figure 8). Careful dislocation observation down the [011] zone axis revealed a large number of dislocations lying on the traces of {111} planes within cell interiors (Figure 14c and d), which were not as apparent in the as-built samples (Figure 4c and d). This suggests that these dislocations formed during cyclic loading and that, as expected, cyclic slip was occurring on {111} planes.

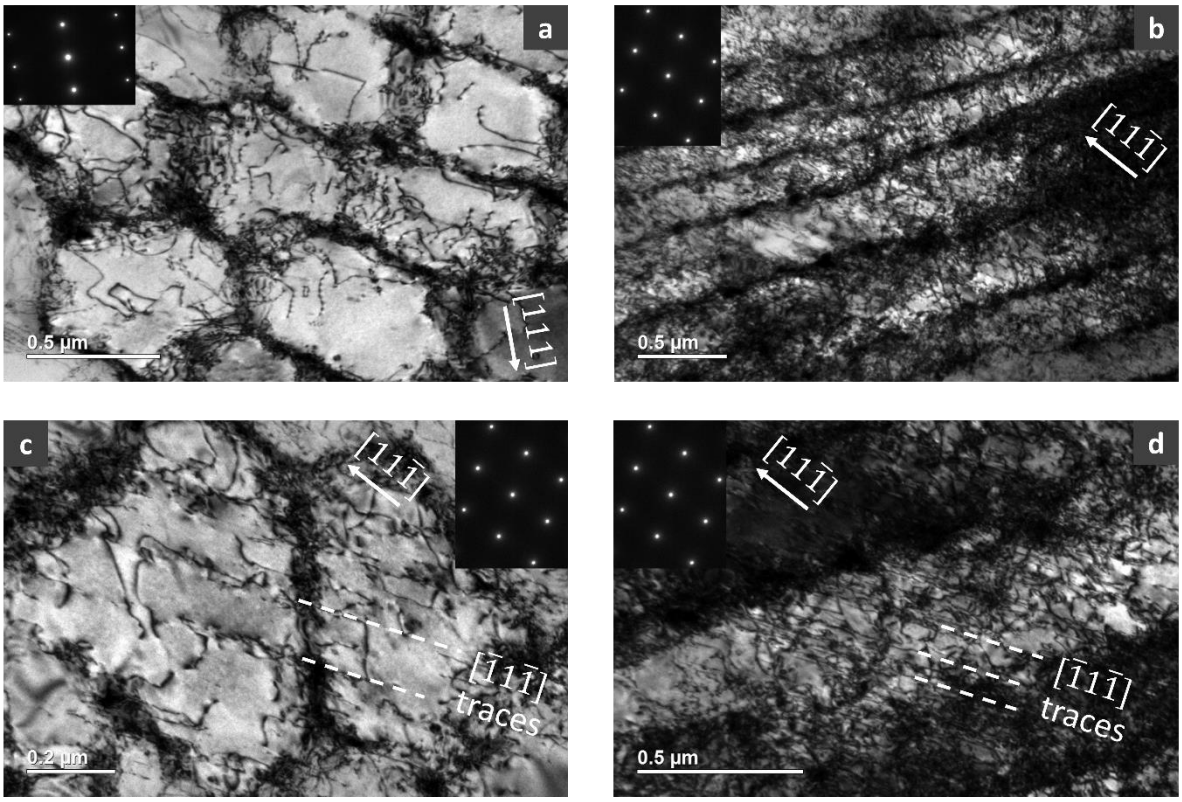


Figure 14: TEM-BF micrographs of the bidirectional sample after fatigue testing at room temperature. Image (a) was obtained with $\boldsymbol{B}=[11\bar{2}]$ *and* $\boldsymbol{g}=[111]$*, while images (b, c, d) were obtained with* $\boldsymbol{B}=[011]$ *and* $\boldsymbol{g}=[11\bar{1}]$*. The foil normal was parallel to the loading direction and thus to SD1 for all micrographs; BD and SD2 were contained in the plane of the foil.*

EBSD scans were performed on the cross sections of the fracture surfaces of the two fatigued test pieces; the resulting maps are shown in Figure 15. Here, the alloy's microstructure appears significantly more similar to that observed in the as-built condition (Figure 2) compared to that after monotonic loading (Figure 9). In particular, the characteristic ordered grain structure of the bidirectional sample is apparent in Figure 15a, indicating that cyclic loading did not have a significant effect on the grain microstructure. Similarly, the textures of the two samples did not evolve significantly during the test; this is apparent when comparing the pole figures of the bidirectional sample after fatigue testing (Figure 15c) with those of the same scanning pattern in the as-built condition (Figure 2g), keeping in mind the different coordinate systems. The lack of a significant modification to the crystallographic textures was likely a consequence of the rather small plastic strains in each cycle (Figure 11d), of the fully-reversed loading and of the short fatigue lives of the two specimens.

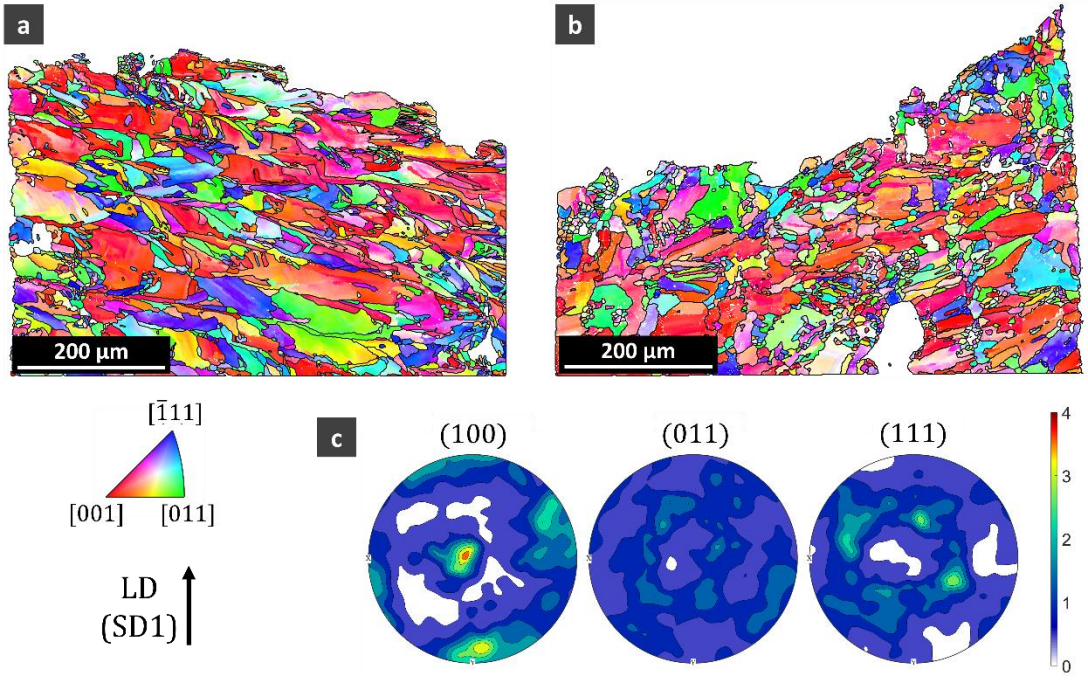


Figure 15: EBSD IPF-LD maps of the cross sections of the bidirectional (a) and chessboard (b) subjected to fatigue testing at room temperature. These scans were performed in the regions right below the fracture surfaces, which are visible at the top of each image. In both cases, the scans include also the lateral edge of the fracture surface; this is found on the left-hand side in (a) and on the right-hand side in (b). Pole figures generated with the data in (a) for the bidirectional sample are shown in (c). The loading direction LD (parallel to SD1) is indicated for reference.

4 DISCUSSION

4.1 SCANNING PATTERNS AND MECHANICAL RESPONSE

The qualitatively similar mechanical responses of the bidirectional and chessboard samples in both monotonic (Figure 6) and cyclic (Figure 11) loading related to the equivalent solidification microstructures and textures in the two samples (Figure 2 and Figure 3), with only slight differences in grain morphologies, grain sizes and solidification cell sizes.

The bidirectional samples exhibited a higher elastic modulus in both monotonic and cyclic loading (Table 3, Figure 11); since the textures generated by the two scanning strategies were very similar (Figure 2g and h, assuming the EBSD scans representative of the overall texture within the builds), the lower elastic modulus of the chessboard samples were mainly associated with their larger porosity fractions, as shown by XCT results (Figure 10). Although such scans were only performed on the fatigue test pieces, poor consolidation was apparent in all chessboard builds examined in this study. The poor consolidation of chessboard builds also explained their lower ductility (Figure 6) and shorter fatigue life (Figure 11c).

The bidirectional samples also exhibited consistently higher yield stresses compared to chessboard samples (Table 3, Figure 11); these related to the differences in both grain size and sub-grain cell size. Finer grain sizes are generally associated with higher yield stresses as described by the Hall-Petch relationship [46]. The yield stress of LPBF alloys has been also found to increase with decreasing sub-grain solidification cell size [10,35,39]. Such effect is attributed to the influence of cell boundaries, which are very effective obstacles to dislocation movement by virtue of their local high dislocation densities (e.g., Figure 4c and d) [20,36]. Finer cellular microstructures provide higher resistance to dislocation motion and therefore higher strength. Indeed, a modified Hall-Petch equation accounting for cell spacing was found to satisfactorily capture the yield strength of LPBF IN718 [10,35], whilst the traditional Hall-Petch relationship accounting for grain size only was found to greatly underestimate the strength of LPBF alloys [39]. The higher yield stress of the bidirectional sample in this study therefore related to both its smaller average grain size (Figure A.1) and smaller average solidification cell size (Figure 3d and f).

4.2 SOLIDIFICATION CELLS AND MONOTONIC RESPONSE

Both samples exhibited pronounced strain hardening during monotonic tensile straining and a rather good ductility (Figure 6). This behaviour related to the fact that the solidification cellular microstructure and the associated dislocation cells were retained throughout straining, as shown by post-mortem TEM

investigations (Figure 8), despite the large strains and associated significant grain rotations observed by EBSD (Figure 9). Dislocation cells could survive large strains thanks to the fact that they are stable configurations, as they minimise the elastic strain energy of the dislocations within them, and to the pinning effect of Laves particles at cell boundaries (Figure 4a and b) [10,36,47]. Dislocation cells therefore kept acting as obstacles for plastic flow through straining, as the dislocation density in the material increased (Figure 8). The increased interactions between mobile dislocations and dislocation cells induces the observed strain hardening [10,35,39]. In turn, the rather good ductility originates from the fact that, whilst acting as obstacles for dislocation glide, dislocation cells do not block slip completely; instead, slip transmission across dislocation cells can occur, upon increasing strain, due to the fact that neighbouring cells have very similar orientations [10,36].

4.3 SOLIDIFICATION CELLS AND CYCLIC RESPONSE

The fatigue response of both samples consisting of initial cyclic hardening followed by cyclic softening until failure (Figure 11c) was qualitatively similar to that of annealed alloys subjected to cyclic loading at room temperature; however, the cyclic hardening phase generally accounts for a larger fraction of the fatigue life in annealed alloys compared to what was observed in this study [48,49]. Cyclic hardening in annealed alloys relates to the gradual increase in the density of dislocations during cyclic loading [50]. Upon further loading, the back and forth movements of dislocations promote dislocation annihilation and, most importantly, the rearrangement of dislocations to form lower energy configurations with alternating high and low dislocation density regions, such as dislocations wall and cell structures [47]; this process is known as dynamic recovery and is driven by a reduction in the overall stored strain energy associated with elastic interactions of dislocations [51,52]. The dynamic recovery of dislocations induces cyclic softening [48,49], due to the generation of very low dislocation density regions, which account for most of the material's volume, where there is little resistance to dislocation glide, and to significant dislocation annihilation upon reversed slip [50].

The very short duration of the cyclic hardening observed in this study (Figure 11c) related to the fact that high dislocation densities were present in the as-built alloy prior to testing, and that such dislocations were already arranged in high/low density configurations (Figure 4c and d) analogous to dislocation cell structures formed during cyclic loading of annealed alloys. Hence, after a very short initial cyclic hardening phase (~20 cycles, Figure 11c) that was induced by an increase in dislocation density within cell interiors [30], the existing dislocation arrangements in the as-built condition favoured the early onset of dislocation dynamic recovery. In turn, dynamic recovery resulted in dislocation annihilation as well as in more well-organised cells (i.e., characterised by lower energetic configurations, as is further discussed below), hence causing gradual cyclic softening until fatigue failure.

The size of the dislocation cells L formed via dynamic recovery in annealed alloys has been shown to be governed by the applied loads, and in particular to be inversely proportional to the resolved shear stress τ according to the similitude relation [51–54]:

$$L = \frac{KGb}{\tau} \tag{1}$$

Where G is the shear modulus, b the Burgers vector of slip dislocations (2.49×10^{-10} m for octahedral slip systems in IN718 [55]) and K is the similitude coefficient. The values of such coefficient commonly reported in the literature vary between K~5 and K~10 [54]. Equation 1 can be used to calculate the dislocation cell size that would be expected to form in the alloy of study. The average resolved shear stress associated with the applied uniaxial stress can be estimated using the average Taylor factor $\bar{M}$. This is a geometrical factor that accounts for the average crystallographic orientation of the grains (i.e., the texture) in a polycrystalline alloy and the consequent orientation of the slip systems within each grain with respect to the applied loads [56–58]. The Taylor factor relates the flow stress σ to the resolved shear stress τ according to [57]:

$$\sigma = \bar{M}\,\tau \tag{2}$$

The average Taylor factors for the bidirectional and chessboard fatigue test pieces were calculated using the MTEX toolbox within MATLAB using the grain orientation data obtained from the top-view EBSD scans shown in Figure 2a and c and were estimated to be 2.86 and 2.87, respectively. The similar values for the two samples related to their analogous crystallographic textures (Figure 2g and h). The shear moduli of the two samples could be calculated from their respective elastic moduli measured in monotonic tensile loading (Table 3) assuming an isotropic elastic behaviour as $G = E/2(1 + \nu)$ [53], where ν is the Poisson's ratio, which was assumed to be equal to 0.3. By substituting the relevant values into Equation 1, the average dislocation cell size according to the similitude relation was estimated to be in the range of 0.325 - 0.65 μm depending on the value of the similitude coefficient *K*.

The cell sizes measured experimentally in both samples in the as-built condition (0.43 ± 0.08 μm and 0.50 ± 0.11 μm for the bidirectional and chessboard samples, respectively) were therefore within the range estimated using the similitude relation. In other words, solidification-induced dislocation cells were morphologically similar to fatigue-induced dislocation cells that would be expected to form as a consequence of the applied loads. It is noted, however, that solidification cells formed due to thermal stressed during deposition cycles rather than due to the back and forth glide of dislocations during cyclic loading; thus, their size was governed by solidification conditions, and in particular by the cooling rate during fabrication and to the pinning effect of particles at cell boundaries. Nonetheless, the similarity between the existing cell sizes and those predicted using the similitude relation was likely a key factor contributing to the stability of such cell structure during cyclic loading, which was apparent in post-mortem TEM investigations (Figure 14). In addition, the stability of the cellular structure was further aided by the pinning effect induced by the fine Laves particles decorating cell boundaries (Figure 4a and b and Figure 5) and by the fact that the movement of mobile dislocation during dynamic recovery was hindered by the constraint exerted by existing cells.

Even though the morphology of as-built solidification cells was rather stable, the evolution of the alloy's cyclic response suggests that dislocations at cell boundaries rearranged during cyclic loading to achieve lower energy configurations. Further insights in this regard can be obtained by considering the evolution of the friction stress and back stress during cyclic loading. The friction stress provides a measure of the

stress required to activate dislocation movement; it is dependent on short-range interactions of dislocations with other dislocations or any other microstructural feature acting as an obstacle to dislocation glide [49]. The back stress, in turn, is associated with long-range internal stresses; in the case of dislocation cell structures formed in cyclic loading, such internal stresses are present even in the unloaded state due to the mismatch between the elastic strains at the interface between cell walls and cell interiors [47]. The back stress increases upon loading, opposing the applied load, as a consequence of plastic strain incompatibilities associated with the different flow stresses in the cell walls and within cell interiors; upon load reversal, the previously-generated back stress acts in the same direction as the applied load, thereby lowering the yield stress (i.e., causing the Bauschinger effect). Upon further straining it rapidly changes sign and starts opposing the applied load until the subsequent load reversal [59]. It can be demonstrated [49,59,60] that the evolution of friction stress σ_E and back stress X during cyclic loading can be calculated from the values of the yield stress σ_y and peak response stress σ_{max} in each cycle as:

$$\sigma_E = \frac{\sigma_{max} + \sigma_y}{2} \tag{3}$$

$$X = \frac{\sigma_{max} - \sigma_y}{2} \tag{4}$$

The evolution of back stress and friction stress throughout the fatigue tests in this study is shown in Figure 16 for both samples together with that of the peak response stress.

The back stress was found to be very high from the beginning of the test in both samples; this was a consequence of the high dislocation densities arranged in dislocation cells in the as-built condition (Figure 4c and d). Even fatigue-induced low-energy dislocation cells induce back stresses in the unloaded state due to elastic strains mismatch [47]. In addition, in the specific case of as-built dislocation cells in the alloy of study, such cells were associated with larger back stresses compared to fatigue-induced dislocation cells since (1) the dislocations forming the cell walls did not have enough time to arrange in low-energy configurations that minimise elastic strain fields (e.g., edge dislocation

dipoles) due to the limited number of thermal cycles during fabrication and (2) the spatial arrangement of such dislocation cells (which is related to grain morphology) was dictated by solidification conditions during fabrication, whilst the spatial arrangement of fatigue-induced cells is driven by the minimisation of the elastic strain fields in a three-dimensional sense [47]. The very high back stresses arising from solidification cells induced yielding upon unloading even before the applied load changed sign within each half-cycle (Figure 11a and b).

Upon cyclic loading, the back stress started decreasing (particularly in the bidirectional sample, Figure 16a) well before the cyclic hardening peak was reached. This was a consequence of the fact that the back and forth glide of dislocations during loading cycles enabled the gradual rearrangement of dislocations within cell walls towards lower-energy configurations. The decrease was, however, rather moderate. This was due to the fact that the spatial arrangement of dislocation cells did not change during loading; this was apparent in both TEM micrographs and EBSD maps (Figure 14 and Figure 15). Hence, even though the dislocations at cell walls rearranged to minimise elastic strain fields (e.g., forming dislocation dipoles), considerable long-range stresses were still present due to the spatial arrangement of solidification cells. Finally, it is worth noting that the decrease in back stress in the chessboard sample was significantly less marked compared to that in the bidirectional sample (Figure 16). This can be explained by considering the higher local substrate temperature within each island induced by the shorter scanning lines in the chessboard sample; such higher temperatures enabled dislocations to rearrange into a lower energy configuration during fabrication, as reflected in the lower initial back stress exhibited by the chessboard sample (Figure 16). Thus, cyclic loading did not induce further significant dislocation rearrangement, leading to a more stable back stress.

The friction stress increased slowly in the first ~20 cycles, reaching a maximum value in the same cycle as the cyclic hardening peak. This was induced by an increase in dislocation density in the early fatigue cycles and the consequent increase in dislocation glide resistance due to interactions with other dislocations. In turn, the increase in dislocation density was dictated by the necessity to accommodate the applied strains. However, once sufficient re-arrangement had occurred and more dislocations became trapped at cell walls, the mobility of dislocations within cell interiors was enhanced, such that

a lower number of dislocations was required to accommodate the applied strain level. Accordingly, the dislocation density started to decrease by annihilation in cell interiors upon load reversal, leading to a decrease in friction stress and thus peak response stress after ~20 cycles in both samples (Figure 16). Glide dislocations could travel greater distances in the chessboard sample due to its larger cell size compared to the bidirectional sample, explaining the more marked decrease in friction stress in the former.

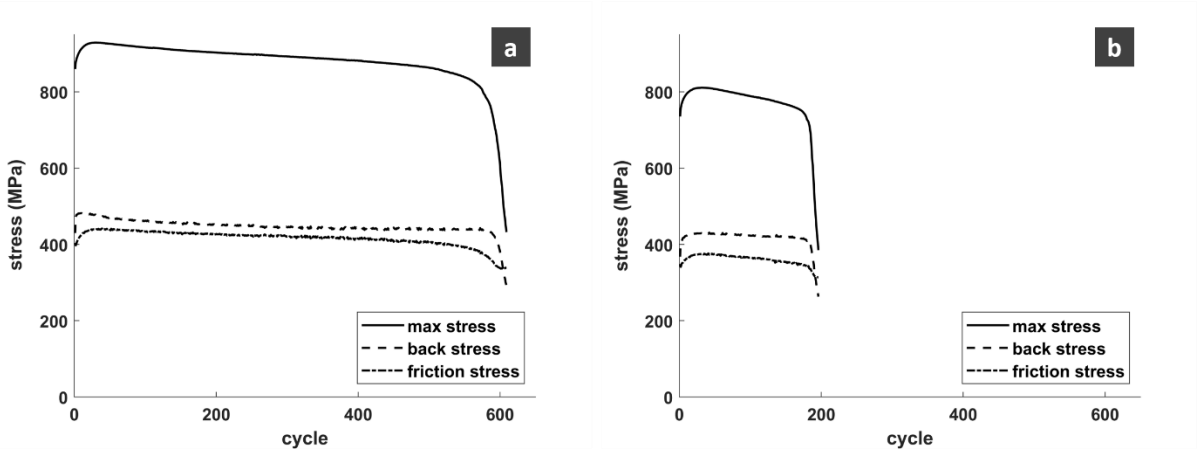


Figure 16: Evolution of maximum stress, back stress and friction stress throughout the fatigue test for the bidirectional sample (a) and the chessboard sample (b).

5 CONCLUSIONS

This study presents a comprehensive investigation of the as-built microstructure and the associated monotonic and fatigue properties at room temperature of IN718 fabricated by laser powder bed fusion using either a bidirectional or a chessboard scanning pattern. Both scanning patterns were shown to result in columnar microstructures, weak cube textures and fine sub-grain solidification cells. In addition, high dislocation densities were observed at cell boundaries, together with several Laves particles and a number of fine carbides. The similar solidification microstructures induced by the two scanning strategies resulted in qualitatively comparable mechanical responses; the higher elastic

modulus and yield strength of bidirectional samples related to their better consolidation and their finer grain and cell sizes compared to chessboard samples.

The alloy's mechanical behaviour was linked to its as-built solidification cellular microstructure. In monotonic tension, cells acted as effective obstacles for dislocation slip, inducing pronounced strain hardening due to the continuously increasing interactions between mobile dislocations and cell walls. In fatigue loading, the early onset of dynamic recovery and cyclic softening was linked to the existing dislocation cells with high dislocation densities in the as-built condition. Solidification cells were shown to be rather stable during cyclic loading, as their size was close to that estimated using the similitude relation for fatigue-induced dislocation cells; the retainment of cells was linked to the rather stable cyclic response of the alloy. The rearrangements of dislocations at cell boundaries as well as their interactions with those within cell interiors were discussed in relation to the evolution of friction stress, back stress and peak response stress during cyclic loading, thereby highlighting their influence on the alloy's cyclic response and explaining the effect of different scanning patterns.

The cellular microstructure characteristic of as-built LPBF IN718 prompts the need for the design of dedicated heat treatment routes. This study for the first time relates the cyclic response of LPBF IN718 to its sub-grain solidification cells, and further links process (scanning pattern and thus local substrate temperature), microstructure (dislocation cell size and their spatial arrangement) and mechanical properties (cyclic response). This study constitutes therefore a first step towards an improved understanding of the influence of solidification cells on the cyclic behaviour of LPBF IN718, potentially paving the way for the development of optimised microstructures for improved fatigue performances.

6 ACKNOWLEDGEMENTS

A. Piglione and M.S.-Pham would like to thank the Beijing Institute of Aeronautical Materials (BIAM) for their support. Most characterisation studies in this work were performed at the BIAM-Imperial Centre for Materials Characterisation, Processing and Modelling at Imperial College London. The authors acknowledge the facilities, as well as the scientific and technical support of the Microscopy

Australia node at The University of Sydney (Sydney Microscopy & Microanalysis). S. Primig is supported by the Australian Research Council DECRA (DE180100440) and UNSW Scientia Fellowship schemes.

7 REFERENCES

[1] Brown EE, Muzyka DR. Nickel-Iron Alloys. High Temp. Mater. Aerosp. Ind. Power, John Wiley & Sons, Ltd; 1987, p. 165–88.

[2] Carlson RG, Radavich JF. Microstructural characterization of cast 718. Proc. Int. Symp. Metall. Appl. Superalloy 718, 1989, p. 79–95.

[3] Warren J, Wei DY. The cyclic fatigue behavior of direct age 718 at 149, 315, 454 and 538 °C. Mater Sci Eng A 2006;428:106–15. https://doi.org/https://doi.org/10.1016/j.msea.2006.04.091.

[4] Popovich VA, Borisov E V, Popovich AA, Sufiiarov VS, Masaylo D V, Alzina L. Impact of heat treatment on mechanical behaviour of Inconel 718 processed with tailored microstructure by selective laser melting. Mater Des 2017;131:12–22. https://doi.org/https://doi.org/10.1016/j.matdes.2017.05.065.

[5] Reed RC. The Superalloys: Fundamentals and Applications. Cambridge: Cambridge University Press; 2006. https://doi.org/10.1017/CBO9780511541285.

[6] Schafrik RE, Ward DD, Groh JR. Application of alloy 718 in GE aircraft engines: past, present and next five years. Proc. Int. Symp. Superalloys Var. Deriv., 2001, p. 1–11. https://doi.org/10.7449/2001/superalloys_2001_1_11.

[7] Parimi LL, A. RG, Clark D, Attallah MM. Microstructural and texture development in direct laser fabricated IN718. Mater Charact 2014;89:102–11. https://doi.org/https://doi.org/10.1016/j.matchar.2013.12.012.

[8] Amato KN, Gaytan SM, Murr LE, Martinez E, Shindo PW, Hernandez J, et al. Microstructures and mechanical behavior of Inconel 718 fabricated by selective laser melting. Acta Mater 2012;60:2229–39. https://doi.org/10.1016/j.actamat.2011.12.032.

[9] Chlebus E, Gruber K, Kuźnicka B, Kurzac J, Kurzynowski T. Effect of heat treatment on the microstructure and mechanical properties of Inconel 718 processed by selective laser melting. Mater Sci Eng A 2015;639:647–55. https://doi.org/https://doi.org/10.1016/j.msea.2015.05.035.

[10] Gallmeyer TG, Moorthy S, Kappes BB, Mills MJ, Amin-Ahmadi B, Stebner AP. Knowledge of process-structure-property relationships to engineer better heat treatments for laser powder bed fusion additive manufactured Inconel 718. Addit Manuf 2020;31:100977. https://doi.org/https://doi.org/10.1016/j.addma.2019.100977.

[11] Zhang D, Niu W, Cao X, Liu Z. Effect of standard heat treatment on the microstructure and mechanical properties of selective laser melting manufactured Inconel 718 superalloy. Mater Sci Eng A 2015;644:32–40. https://doi.org/https://doi.org/10.1016/j.msea.2015.06.021.

[12] Attard B, Cruchley S, Beetz C, Megahed M, Chiu YL, Attallah MM. Microstructural control during laser powder fusion to create graded microstructure Ni-superalloy components. Addit Manuf 2020;36:101432. https://doi.org/https://doi.org/10.1016/j.addma.2020.101432.

[13] Yadollahi A, Shamsaei N. Additive manufacturing of fatigue resistant materials: Challenges and opportunities. Int J Fatigue 2017;98:14–31. https://doi.org/10.1016/j.ijfatigue.2017.01.001.

[14] DebRoy T, Wei HL, Zuback JS, Mukherjee T, Elmer JW, Milewski JO, et al. Additive manufacturing of metallic components – Process, structure and properties. Prog Mater Sci 2018;92:112–224. https://doi.org/https://doi.org/10.1016/j.pmatsci.2017.10.001.

[15] Pei C, Shi D, Yuan H, Li H. Assessment of mechanical properties and fatigue performance of a selective laser melted nickel-base superalloy Inconel 718. Mater Sci Eng A 2019;759:278–87. https://doi.org/https://doi.org/10.1016/j.msea.2019.05.007.

[16] Sangid MD, Book TA, Naragani D, Rotella J, Ravi P, Finch A, et al. Role of heat treatment

and build orientation in the microstructure sensitive deformation characteristics of IN718 produced via SLM additive manufacturing. Addit Manuf 2018;22:479–96. https://doi.org/https://doi.org/10.1016/j.addma.2018.04.032.

[17] Witkin DB, Patel DN, Bean GE. Notched fatigue testing of Inconel 718 prepared by selective laser melting. Fatigue Fract Eng Mater Struct 2019;42:166–77. https://doi.org/https://doi.org/10.1111/ffe.12880.

[18] Konečná R, Kunz L, Nicoletto G, Bača A. Long fatigue crack growth in Inconel 718 produced by selective laser melting. Int J Fatigue 2016;92:499–506. https://doi.org/https://doi.org/10.1016/j.ijfatigue.2016.03.012.

[19] Wan HY, Luo YW, Zhang B, Song ZM, Wang LY, Zhou ZJ, et al. Effects of surface roughness and build thickness on fatigue properties of selective laser melted Inconel 718 at 650 °C. Int J Fatigue 2020;137:105654. https://doi.org/https://doi.org/10.1016/j.ijfatigue.2020.105654.

[20] Yoo YSJ, Book TA, Sangid MD, Kacher J. Identifying strain localization and dislocation processes in fatigued Inconel 718 manufactured from selective laser melting. Mater Sci Eng A 2018;724:444–51. https://doi.org/https://doi.org/10.1016/j.msea.2018.03.127.

[21] Konečná R, Nicoletto G, Kunz L, Bača A. Microstructure and directional fatigue behavior of Inconel 718 produced by selective laser melting. Procedia Struct Integr 2016;2:2381–8. https://doi.org/https://doi.org/10.1016/j.prostr.2016.06.298.

[22] Sabelkin VP, Cobb GR, Shelton TE, Hartsfield MN, Newell DJ, O'Hara RP, et al. Mitigation of anisotropic fatigue in nickel alloy 718 manufactured via selective laser melting. Mater Des 2019;182:108095. https://doi.org/https://doi.org/10.1016/j.matdes.2019.108095.

[23] Ardi DT, Guowei L, Maharjan N, Mutiargo B, Leng SH, Srinivasan R. Effects of post-processing route on fatigue performance of laser powder bed fusion Inconel 718. Addit Manuf 2020;36:101442. https://doi.org/https://doi.org/10.1016/j.addma.2020.101442.

[24] Kim S, Choi H, Lee J, Kim S. Room and elevated temperature fatigue crack propagation behavior of Inconel 718 alloy fabricated by laser powder bed fusion. Int J Fatigue 2020;140:1–10. https://doi.org/https://doi.org/10.1016/j.ijfatigue.2020.105802.

[25] Sui S, Chen J, Fan E, Yang H, Lin X, Huang W. The influence of Laves phases on the high-cycle fatigue behavior of laser additive manufactured Inconel 718. Mater Sci Eng A 2017;695:6–13. https://doi.org/https://doi.org/10.1016/j.msea.2017.03.098.

[26] Balachandramurthi AR, Moverare J, Dixit N, Pederson R. Influence of defects and as-built surface roughness on fatigue properties of additively manufactured Alloy 718. Mater Sci Eng A 2018;735:463–74. https://doi.org/https://doi.org/10.1016/j.msea.2018.08.072.

[27] Komarasamy M, Shukla S, Williams S, Kandasamy K, Kelly S, Mishra RS. Microstructure, fatigue, and impact toughness properties of additively manufactured nickel alloy 718. Addit Manuf 2019;28:661–75. https://doi.org/https://doi.org/10.1016/j.addma.2019.06.009.

[28] Aydinöz ME, Brenne F, Schaper M, Schaak C, Tillmann W, Nellesen J, et al. On the microstructural and mechanical properties of post-treated additively manufactured Inconel 718 superalloy under quasi-static and cyclic loading. Mater Sci Eng A 2016;669:246–58. https://doi.org/10.1016/j.msea.2016.05.089.

[29] Tucho WM, Cuvillier P, Sjolyst-Kverneland A, Hansen V. Microstructure and hardness studies of Inconel 718 manufactured by selective laser melting before and after solution heat treatment. Mater Sci Eng A 2017;689:220–32. https://doi.org/10.1016/j.msea.2017.02.062.

[30] Jin M, Piglione A, Dovgyy B, Hosseini E, Hooper PA, Holdsworth SR, et al. Cyclic plasticity and fatigue damage of CrMnFeCoNi high entropy alloy fabricated by laser powder-bed fusion. Addit Manuf 2020;36:101584. https://doi.org/https://doi.org/10.1016/j.addma.2020.101584.

[31] Dovgyy B, Piglione A, Hooper PA, Pham M-S. Comprehensive assessment of the printability of CoNiCrFeMn in Laser Powder Bed Fusion. Mater Des 2020;194:108845. https://doi.org/https://doi.org/10.1016/j.matdes.2020.108845.

[32] Piglione A, Dovgyy B, Liu C, Gourlay CM, Hooper PA, Pham MS. Printability and microstructure of the CoCrFeMnNi high-entropy alloy fabricated by laser powder bed fusion. Mater Lett 2018;224C:22–5. https://doi.org/10.1016/j.matlet.2018.04.052.

[33] Kong D, Dong C, Wei S, Ni X, Zhang L, Li R, et al. About metastable cellular structure in additively manufactured austenitic stainless steels. Addit Manuf 2021;38:101804. https://doi.org/https://doi.org/10.1016/j.addma.2020.101804.

[34] Zhang D, Feng Z, Wang C, Wang W, Liu Z, Niu W. Comparison of microstructures and mechanical properties of Inconel 718 alloy processed by selective laser melting and casting. Mater Sci Eng A 2018;724:357–67. https://doi.org/https://doi.org/10.1016/j.msea.2018.03.073.

[35] Zhu ZG, Nguyen QB, Ng FL, An XH, Liao XZ, Liaw PK, et al. Hierarchical microstructure and strengthening mechanisms of a CoCrFeNiMn high entropy alloy additively manufactured by selective laser melting. Scr Mater 2018;154:20–4. https://doi.org/https://doi.org/10.1016/j.scriptamat.2018.05.015.

[36] Liu L, Ding Q, Zhong Y, Zou J, Wu J, Chiu Y-L, et al. Dislocation network in additive manufactured steel breaks strength–ductility trade-off. Mater Today 2018;21:354–61. https://doi.org/https://doi.org/10.1016/j.mattod.2017.11.004.

[37] Hielscher R, Schaeben H. A novel pole figure inversion method: specification of the MTEX algorithm. J Appl Crystallogr 2008;41:1024–37. https://doi.org/https://doi.org/10.1107/S0021889808030112.

[38] Gault B, Moody MP, Cairney JM, Ringer SP. Atom probe microscopy. New York: Springer; 2012. https://doi.org/10.1007/978-1-4614-3436-8.

[39] Wang YM, Voisin T, McKeown JT, Ye J, Calta NP, Li Z, et al. Additively manufactured hierarchical stainless steels with high strength and ductility. Nat Mater 2018;17:63–71. https://doi.org/10.1038/nmat5021.

[40] Prashanth KG, Eckert J. Formation of metastable cellular microstructures in selective laser

melted alloys. J Alloys Compd 2017;707:27–34. https://doi.org/https://doi.org/10.1016/j.jallcom.2016.12.209.

[41] DuPont JN, Marder AR, Notis MR, Robino C V. Solidification of Nb-bearing superalloys: Part II. Pseudoternary solidification surfaces. Metall Mater Trans A 1998;29:2797–806. https://doi.org/10.1007/s11661-998-0320-x.

[42] Theska F, Ringer SP, Primig S. Atom Probe Microscopy of Strengthening Effects in Alloy 718. Microsc Microanal 2019;25:470–80. https://doi.org/10.1017/S1431927618015611.

[43] ASTM F3055-14a, Standard Specification for Additive Manufacturing Nickel Alloy (UNS N07718) with Powder Bed Fusion, ASTM International, West Conshohocken, PA, 2014, www.astm.org n.d. https://doi.org/10.1520/F3055-14A.

[44] Bowen DK, Christian JW. The calculation of shear stress and shear strain for double glide in tension and compression. Philos Mag A J Theor Exp Appl Phys 1965;12:369–78. https://doi.org/10.1080/14786436508218879.

[45] Carter LN, Martin C, Withers PJ, Attallah MM. The influence of the laser scan strategy on grain structure and cracking behaviour in SLM powder-bed fabricated nickel superalloy. J Alloys Compd 2014;615:338–47. https://doi.org/https://doi.org/10.1016/j.jallcom.2014.06.172.

[46] Li Y, Bushby AJ, Dunstan DJ. The Hall-Petch effect as a manifestation of the general size effect. Proc R Soc A Math Phys Eng Sci 2016;472:20150890. https://doi.org/10.1098/rspa.2015.0890.

[47] Mughrabi H. Dislocation wall and cell structures and long-range internal stresses in deformed metal crystals. Acta Metall 1983;31:1367–79. https://doi.org/https://doi.org/10.1016/0001-6160(83)90007-X.

[48] Pham MS, Holdsworth SR. Role of microstructural condition on fatigue damage development of AISI 316L at 20 and 300°C. Int J Fatigue 2013;51:36–48. https://doi.org/10.1016/j.ijfatigue.2013.02.005.

[49] Pham MS, Holdsworth SR, Janssens KGF, Mazza E. Cyclic deformation response of AISI 316L at room temperature: Mechanical behaviour, microstructural evolution, physically-based evolutionary constitutive modelling. Int J Plast 2013;47:143–64. https://doi.org/https://doi.org/10.1016/j.ijplas.2013.01.017.

[50] Pham MS, Solenthaler C, Janssens KGF, Holdsworth SR. Dislocation structure evolution and its effects on cyclic deformation response of AISI 316L stainless steel. Mater Sci Eng A 2011;528:3261–9. https://doi.org/10.1016/j.msea.2011.01.015.

[51] Kuhlmann-Wilsdorf D, Van Der Merwe JH. Theory of dislocation cell sizes in deformed metals. Mater Sci Eng 1982;55:79–83. https://doi.org/https://doi.org/10.1016/0025-5416(82)90086-6.

[52] Prinz F, Argon AS. Dislocation cell formation during plastic deformation of copper single crystals. Phys Status Solidi A 1980;57:741–53. https://doi.org/https://doi.org/10.1002/pssa.2210570234.

[53] Staker MR, Holt DL. The dislocation cell size and dislocation density in copper deformed at temperatures between 25 and 700°C. Acta Metall 1972;20:569–79. https://doi.org/https://doi.org/10.1016/0001-6160(72)90012-0.

[54] Sauzay M, Kubin LP. Scaling laws for dislocation microstructures in monotonic and cyclic deformation of fcc metals. Prog Mater Sci 2011;56:725–84. https://doi.org/https://doi.org/10.1016/j.pmatsci.2011.01.006.

[55] Ghorbanpour S, Zecevic M, Kumar A, Jahedi M, Bicknell J, Jorgensen L, et al. A crystal plasticity model incorporating the effects of precipitates in superalloys: Application to tensile, compressive, and cyclic deformation of Inconel 718. Int J Plast 2017;99:162–85. https://doi.org/https://doi.org/10.1016/j.ijplas.2017.09.006.

[56] Thijs L, Montero Sistiaga ML, Wauthle R, Xie Q, Kruth J-P, Van Humbeeck J. Strong morphological and crystallographic texture and resulting yield strength anisotropy in selective

laser melted tantalum. Acta Mater 2013;61:4657–68. https://doi.org/https://doi.org/10.1016/j.actamat.2013.04.036.

[57] Tome C, Canova GR, Kocks UF, Christodoulou N, Jonas JJ. The relation between macroscopic and microscopic strain hardening in F.C.C. polycrystals. Acta Metall 1984;32:1637–53. https://doi.org/https://doi.org/10.1016/0001-6160(84)90222-0.

[58] Mecking H, Kocks UF, Hartig C. Taylor factors in materials with many deformation modes. Scr Mater 1996;35:465–71. https://doi.org/10.1016/1359-6462(96)00137-6.

[59] Kuhlmann-Wilsdorf D, Laird C. Dislocation behavior in fatigue II. Friction stress and back stress as inferred from an analysis of hysteresis loops. Mater Sci Eng 1979;37:111–20. https://doi.org/https://doi.org/10.1016/0025-5416(79)90074-0.

[60] Cottrell AH. Dislocations and plastic flow in crystals. New York: Oxford University Press; 1953.

APPENDIX

A.1 GRAIN SIZE DISTRIBUTION

The grain size distributions for the bidirectional and chessboard samples obtained from top view and side view EBSD maps (Figure 2) are shown in Figure A.1. Very few grains in each map were found to be larger than 60 μm; these have been included in the last bin in each histogram.

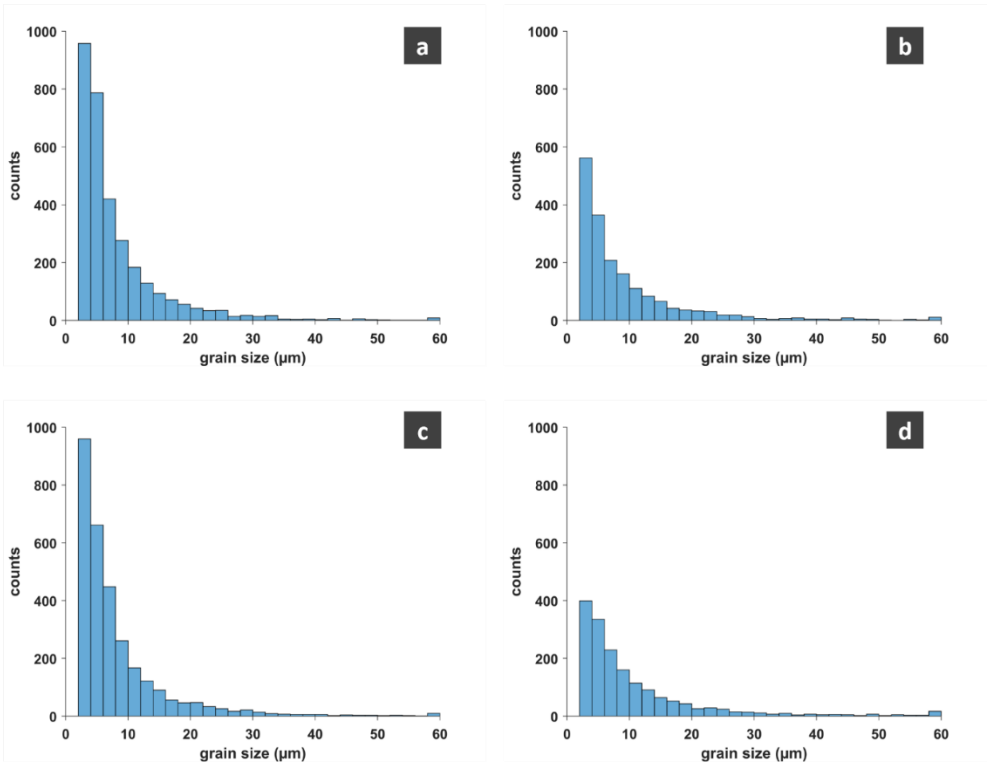


Figure A.1: Grain size distributions obtained from the EBSD maps shown in Figure 2: (a) bidirectional top view, (b) bidirectional side view, (c) chessboard top view, (d) chessboard side view. Few grains in each map were larger than 60 µm; these have been included in the last bin of each histogram.

A.2 PROXIGRAMS

Proxigrams showing the variation in elemental composition across the matrix/Laves interface and across the matrix/carbide interface obtained from the APT dataset shown in Figure 5a-c are shown in Figure A.2. Such analysis was performed on a bidirectional sample in the as-built condition.

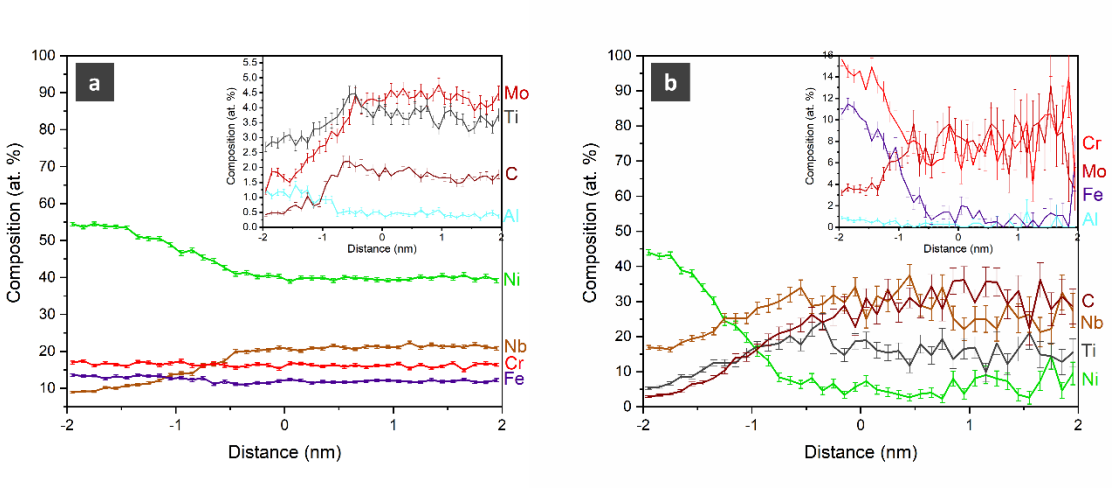


Figure A.2: Proxigrams showing the variation in elemental composition across the matrix/Laves interface (a) and across the matrix/carbide interface (b) in a bidirectional sample in the as-built condition. In both images the interface is located at zero on the x-axis and the matrix is found on the left-hand side. The insets show magnified views of the proxigrams for elements present in low concentrations. These proxigrams were obtained from the same APT dataset shown in Figure 5a-c.